

**Key Points:**

- We present a quantitative analysis integrating geodetic, geological and seismological observations in Tierra del Fuego
- Twenty-four years of Global Navigation Satellite System observations constrain fault geometry and simulated viscoelastic relaxation decades after the 1949 earthquake
- Agreement is achieved between current geodetic deformation rates and the long-term geologic slip rate across the Magallanes-Fagnano Fault

**Supporting Information:**

Supporting Information may be found in the online version of this article.

**Correspondence to:**






L. P. O. Mendoza,  
[lmendoza@fcaglp.unlp.edu.ar](mailto:lmendoza@fcaglp.unlp.edu.ar)

**Citation:**

Mendoza, L. P. O., Richter, A., Marderwald, E. R., Hormaechea, J. L., Connon, G., Scheinert, M., et al. (2022). Horizontal and vertical deformation rates linked to the Magallanes-Fagnano Fault, Tierra del Fuego: Reconciling geological and geodetic observations by modeling the current seismic cycle. *Tectonics*, 41, e2021TC006801. <https://doi.org/10.1029/2021TC006801>

Received 8 MAR 2021  
Accepted 26 NOV 2021

## Horizontal and Vertical Deformation Rates Linked to the Magallanes-Fagnano Fault, Tierra Del Fuego: Reconciling Geological and Geodetic Observations by Modeling the Current Seismic Cycle

L. P. O. Mendoza<sup>1,2</sup> , A. Richter<sup>1,2,3</sup> , E. R. Marderwald<sup>1,2</sup> , J. L. Hormaechea<sup>2,4,5</sup> , G. Connon<sup>2,4</sup>, M. Scheinert<sup>3</sup> , R. Dietrich<sup>3</sup>, and R. A. Perdomo<sup>2,5</sup>

<sup>1</sup>Laboratorio de Meteorología espacial, Atmósfera terrestre, Geodesia, Geodinámica, diseño de Instrumental y Astrometría (MAGGIA), Facultad de Ciencias Astronómicas y Geofísicas (FCAG), Universidad Nacional de La Plata (UNLP), La Plata, Argentina, <sup>2</sup>Consejo Nacional de Investigaciones Científicas y Técnicas (CONICET), Buenos Aires, Argentina, <sup>3</sup>Institut für Planetare Geodäsie (IPG), Technische Universität Dresden (TUD), Dresden, Germany, <sup>4</sup>Estación Astronómica Río Grande (EARG), Río Grande, Argentina, <sup>5</sup>Facultad de Ciencias Astronómicas y Geofísicas (FCAG), Universidad Nacional de La Plata (UNLP), La Plata, Argentina

**Abstract** We integrate geodetic, geological and seismological observations in Tierra del Fuego, into a consistent and quantitative analysis, to better understand the current crustal deformation associated to the Magallanes-Fagnano Fault, that is, the transform boundary between the South American and Scotia plates at the southern tip of Patagonia. To obtain reliable geodetic estimates of the thickness of the seismogenic layer, we model the current seismic cycle from the great 1949  $M_w \approx 7.7$  earthquake to the present, including the lasting effects of postseismic relaxation. The model parameters are constrained by Global Navigation Satellite System velocities obtained by reprocessing 24 years of observations in the island with up-to-date models and satellite products. We combine the observed deformation rates with long-term geological estimates of the slip rate in this transform system during the Holocene. The modeling results point to a seismogenic layer thickness of  $15 \pm 3$  km and to fault planes inclined  $63^\circ \pm 4^\circ$ , dipping to the South. Along the sections of the Magallanes-Fagnano Fault in the island these results are consistent with a seismic moment deficit rate, per unit of length, of  $3.2 \pm 0.8 \times 10^{12}$  N m a<sup>-1</sup> km<sup>-1</sup>, and a cumulative seismic moment, to date, equivalent to an earthquake of magnitude  $M_w \approx 7$ . The postseismic viscoelastic relaxation, probably related to viscous flow in the mantle, affects the entire region up to  $\sim 200$  km away from the Magallanes-Fagnano Fault, and more than 60 years after the earthquake.

### 1. Introduction

The Magallanes-Fagnano Fault System (MFS), which extends over nearly 600 km and runs across the Tierra del Fuego island (TDF, shared between Chile and Argentina), constitutes the left-lateral transform boundary between the South American (SA) and Scotia (SC) plates at the southern tip of Patagonia (Klepeis, 1994; Lodolo et al., 2003; Tassone et al., 2005). The fault system is composed of several structures, including the main Magallanes-Fagnano Fault (MF) and the Deseado Fault (DF) along both of which Quaternary tectonic activity has been documented (e.g., Costa et al., 2006; Klepeis, 1994; Lodolo et al., 2003; Menichetti et al., 2008; Roy et al., 2019; Sandoval & De Pascale, 2020). In particular, Lodolo et al. (2003) identified several en échelon segments of the MF, linked by fault jogs, and running mostly underwater across the Strait of Magellan (SM) and along Lake Fagnano (LF), until reaching the Atlantic Ocean (Figure 1). In fact, this narrow, 105 km long lake has been interpreted as composed of spindle-shaped pull-apart sub-basins associated to parallel segments of the MF (Esteban et al., 2014; Lodolo et al., 2003; Mann, 2007). In addition, Diraison et al. (1997) and Menichetti et al. (2008) propose that extensional tectonic structures in the northern part of Tierra del Fuego, the most prominent being the Inútil Bay and San Sebastián Bay graben (IB–SSB, Figure 1), accommodate parts of the relative motion between the SA and the SC plates. De Pascale (2021) makes a similar suggestion, regarding an extensional tectonic setting in and around SM to the east and northeast of MFS, when commenting on a paper by Santibáñez et al. (2018) related to seismic risk in Chile. Robust geodetic observations, such as those obtained in the present work, may contribute to a better characterization of the regional geological setting.

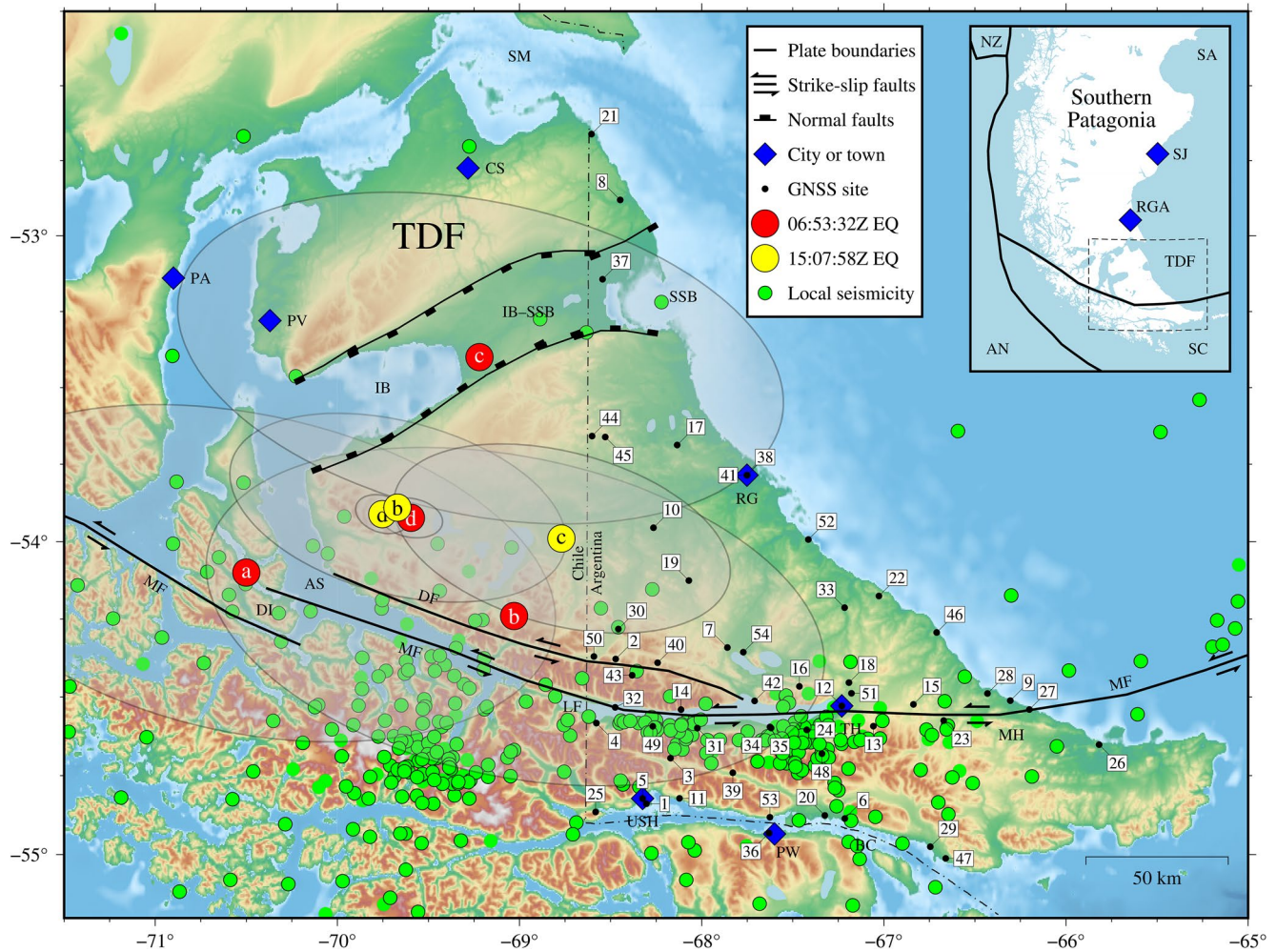


**Figure 1.** Location of all Global Navigation Satellite System sites used for model parameter calibration (the numbers correspond to entries in Table 1); estimated epicenters for the two damaging earthquakes that occurred in Tierra del Fuego on 17 December 1949, according to (a) Zamarbide and Castano (1978), (b) Jaschek et al. (1982), (c) Pelayo and Wiens (1989) and (d) Bondár et al., 2015 (updated 2020-07-10), only Bondár et al. (2015) and Pelayo and Wiens (1989) provide error ellipses (90% confidence, i.e., two sigmas), thus we associate here Pelayo & Wiens's ellipses to the earlier inferences, made by Zamarbide and Castano (1978) and Jaschek et al. (1982), to show the most consistent location for both epicenters; approximate traces of Magallanes-Fagnano Fault and Deseado Fault adapted from Lodolo et al. (2003), Roy et al. (2019) and Sandoval and De Pascale (2020) and normal faults limiting the Inútil Bay and San Sebastián Bay (IB-SSB) graben adapted from Diraison et al. (1997) and Menichetti et al. (2008); local seismicity registered between January 2010 and December 2020, with local magnitudes  $M_l$  between 2 and 5.3 (Connon et al., 2021; Sabbione et al., 2007, 2017). Inset: Tectonic setting for southernmost South America (Bird, 2003). Other acronyms used: AN (Antarctic Plate), AS (Almirantazgo Sound), BC (Beagle Channel), CS (Cerro Sombrero), DI (Dawson Island), IB (Inútil Bay), LF (Lake Fagnano), MH (Malengüena Hill), NZ (Nazca Plate), PA (Punta Arenas), PV (Porvenir), PW (Puerto Williams), RG (Río Grande), RGA (Río Gallegos), SA (South American Plate), SSB (San Sebastián Bay), SC (Scotia Plate), SJ (San Julián), SM (Strait of Magellan), TH (Tolhuin), USH (Ushuaia).

There have been several estimates of the magnitude of relative motion being accommodated during the Holocene across the MFS (e.g., DeMets et al., 2010; L. Mendoza et al., 2015; Roy et al., 2019; Sandoval & De Pascale, 2020; Smalley et al., 2003, all discussed later). So far, many studies, based on geological or geodetic observations, point to the MFS being a slow tectonic boundary, according to the classification proposed by Stirling et al. (2013) for slip rates  $\dot{s} < 10 \text{ mm a}^{-1}$ . Over a decade of records from a regional network of broadband seismic stations in Tierra del Fuego, and continental Patagonia, indicate low-magnitude (i.e., local magnitudes  $M_l$  between 2 and 5.3) and shallow seismicity associated with the MFS sections in the island (e.g., Ammirati et al., 2020; Febrer et al., 2000). The average focal depth is less than 10 km and the epicenters are mainly localized south of the MF trace (e.g., Ammirati et al., 2020; Buffoni et al., 2009; Febrer et al., 2000). Although significant advances have recently been made in the regional modeling of the wave velocity of the crust (e.g., Ammirati et al., 2020; Buffoni et al., 2017) the suboptimal number and distribution of seismic stations still appear to impede reliable hypocenter determinations (Ammirati et al., 2020). The geographic distribution of events recorded over

more than one decade (Connon et al., 2021; Sabbione et al., 2007, 2017), and the recent determination of the focal mechanism associated with an earthquake along the MF (Bollini, 2021), help to choose between the various fault models obtained in this work based on the inversion of the geodetic observations.

On the other hand, the MFS has been identified as the most likely source of seismic hazard in Tierra del Fuego, based on prehistoric and historical records of damaging earthquakes (González Bonorino et al., 2011; Martinić Beroš, 2008; Perucca et al., 2015). The largest instrumentally recorded event, to date, occurred on 17 December 1949, when two earthquakes with moment magnitudes  $M_w$  about  $\sim 7.7$  and  $\sim 7.3$  were felt at Ushuaia, Río Grande, Punta Arenas and even Río Gallegos and San Julian, 350 and 600 km north on continental Patagonia, respectively (ISC-GEM catalog, events 8,97,093 and 8,97,095, Bondár et al., 2015; Di Giacomo et al., 2015, 2018). Several estimates of both epicenters and moment magnitudes have been derived over the years from teleseismic records, resulting in consistent but weakly constrained relocations (Bondár et al., 2015; Jaschek et al., 1982; Pelayo & Wiens, 1989; Zamarbide & Castano, 1978, see Figure 1). In addition, some studies attribute a significantly higher magnitude to the first earthquake at 6:53 UTC that day (e.g., Ammirati et al., 2020; Bondár et al., 2015; Pelayo & Wiens, 1989; Zamarbide & Castano, 1978), others attribute a stronger magnitude to the second earthquake at 15:08 UTC (e.g., Buffoni et al., 2019; Febrer et al., 2000; Jaschek et al., 1982; Lomnitz, 1970; Perucca et al., 2015), and still others suggest that both events were of similar magnitude (e.g., Abascal & González Bonorino, 2014; Costa et al., 2006; González Bonorino et al., 2011; Roy et al., 2019). Prior to these events, the largest earthquake historically recorded in Tierra de Fuego occurred on 1 February 1879 (or February 2nd, depending on the cited source), with an estimated magnitude between 7 and 7.5 (Lomnitz, 1970; Martinić Beroš, 2008). By studying disturbed trees, Pedrera et al. (2014) inferred that both ruptures, in 1879 and 1949, occurred along MF including sections east of Lake Fagnano. After the large 1949 events, and their aftershocks during the following year, the only regional earthquake with a magnitude greater than six occurred on 15 June 1970. This event had a moment magnitude  $M_w \simeq 7.2$  and a focal depth of  $\sim 10$  km, with epicenter in the ocean, more than 100 km east of the shores of the island (ISC-GEM catalog, event iscgem794605, Bondár et al., 2015; Di Giacomo et al., 2015, 2018). Most studies do agree in attributing the source of both events in 1949 to ruptures along the MF in Tierra del Fuego (Figure 1). Nevertheless, the exact focal location and the length of the ruptures have never been precisely determined. In the present work we address most of the controversial and not precisely known characteristics of the largest of the 1949 earthquakes (i.e., magnitude, rupture length, focal point), augmenting seismological and geological evidence with accurate geodetic observations. The joint analysis of all these data together provides a more complete picture of the event and its lasting effects along this section of the plate boundary.

We present here a new set of Global Navigation Satellite System (GNSS) observations in Tierra del Fuego, since 1994, which includes for the first time reliable geodetic determinations of current vertical deformation rates. These rates are based on almost  $2 \times 10^5$  daily position solutions at 54 sites in TDF. The vertical rates allow for a consistent analysis with independent data, for example, local geologic and geophysical measurements and models or satellite observations. In turn, making use of this GNSS data set, we construct a numerical model of the current seismic cycle in Tierra del Fuego, from the last damaging earthquake in 1949 to the present, simultaneously consistent with available geological and seismological observations. We seek to quantify the effect of the postseismic relaxation process at present and its impact on the estimation of the interseismic locking depth of MF sections in the island. These geodetically inferred depths constitute reliable indicators of seismic potential, given their correlation with the thickness of the seismogenic layer (Wright et al., 2013). In fact, this is a topic of great interest in Tierra del Fuego, on both sides of the border between Argentina and Chile. For example, a reassessment of the seismic risk in some areas of the island has been suggested, based on simulations of earthquakes similar to the one that occurred in 1949 and taking into account the current urban development (Abascal & González Bonorino, 2014). In our modeling effort we aim to reconcile the geodetically observed deformation rates in the island, both horizontal and vertical, with geological studies. On the one hand, geodetic and geological slip rate estimates across the MF should coincide (Meade et al., 2013), given that the geodetic observations have been obtained well before the eventual end of the current seismic cycle, although discrepancies between the results of both methods have been discussed for diverse faults (e.g., Tong et al., 2014; Zeng & Shen, 2014). On the other hand, reliable determinations of vertical GNSS velocities now make it possible to test the existence of movement related to tectonic uplift across the MFS, as well as to extensional structures proposed to the north of the island (e.g., De Pascale, 2021; Diraison et al., 1997).



## 2. Data and Methods

### 2.1. A Quarter Century of GNSS Observations in Tierra Del Fuego

The geodetic data consists of raw GNSS observations covering 24 years, between 1994 and 2018, with a weighted mean epoch  $t_{\text{GNSS}} \approx 2010$ . Although it constitutes a heterogeneous set, including early episodic occupations as well as data from more recent semi-permanent and permanent GNSS stations, we are able to apply a consistent analysis strategy for all sites, and over the entire time period. These data include four field campaigns carried out in the island since 2017, which complement the data collected before 2015 and used in previous studies (L. Mendoza et al., 2011; L. Mendoza et al., 2015). The only exception is the earliest available observations, dating back to 1993, which are not included in this analysis because they fall outside the time frame of the GNSS products used (i.e., precise satellite orbits and clocks). The episodic and semi-permanent observations are complemented with data from continuously operating stations administered by the International GNSS Service (IGS, Johnston et al., 2017), the Instituto Geográfico Nacional (IGN, Argentina, Piñón et al., 2018) and the Centro Sismológico Nacional (CSN, Chile, Barrientos et al., 2018). In total, 54 regional GNSS sites are included in this work (Figure 1).

In our previous works we employed a differential GNSS analysis method for the computation of the daily position solutions. This approach requires the introduction of a global or a regional reference frame (RF) realization by means of constraints on coordinates or on Helmert transformation parameters. The consistency and stability of the chosen RF, both in space and over a long time period, as well as the number and distribution of constraining reference sites near the study area, have an impact on the quality of the daily solutions and the derived parameters (e.g., the deformation rates). The more stable the RF realization is, the less scatter or noise leaks into the station coordinates time series (Bevis & Brown, 2014). This issue, that could include low frequency components (i.e., drifts), is known as the *RF realization error* (Dietrich et al., 2001). In fact, this constitutes a real challenge for an analysis of multi-decadal GNSS observations in Tierra del Fuego, and in Patagonia in general, due to the lack of sufficient and well distributed reference sites, spanning the entire time frame, and the numerous episodic coordinate changes produced by seismic activity.

In order to overcome the issue described above we decided to apply a precise point positioning (PPP) processing strategy (Zumberge et al., 1997), made possible by the recent availability of highly accurate and consistent GNSS satellite products (Griffiths, 2018). In particular, we employ the jp2 time series produced by the Jet Propulsion Laboratory (USA) in the frame of the IGS repro2 campaign. Therefore, the resulting position time series are aligned to the IGS14 RF (Rebischung & Schmid, 2016), as materialized by the jp2 satellite products. In practice, the position time series for each site were computed using the Bernese GNSS Software package (BSW, Dach et al., 2015). First order ionospheric delays are eliminated by means of the ionosphere-free linear combination and higher-order terms are modeled by the analysis software according to Fritsche et al. (2005). We model at the observation level the deformation produced by oceanic (model GOT4.8; Ray, 1999) and atmospheric (van Dam & Ray, 2010) tidal loading at each site. In addition, the tropospheric delays are accounted for, including hourly zenith delay and gradient estimates (Chen & Herring, 1997), modeled with the Vienna Mapping Function 1 (VMF1, Boehm et al., 2006).

### 2.2. Estimation of Trajectory Models

To estimate horizontal and vertical deformation rates at each site, with reliable variances, we apply the concept of station trajectory models (see also Bevis & Brown, 2014). Following the methods explained in Montillet and Bos (2020) we estimate site-specific models, carefully tuned to the particular time range, sampling rate and number of available observations in each position time series. In practice, we apply the Maximum Likelihood Estimation method, using the HECTOR tool (Bos et al., 2012). We model the trajectories of the sites as

$$\mathbf{x}(t) = \mathbf{x}_0 + \mathbf{v}(t - t_0) + \sum_{j=1}^{n_j} \mathbf{b}_j H(t - t_j) + \sum_{k=1}^{n_F} (\mathbf{s}_k \sin(\omega_k t) + \mathbf{c}_k \cos(\omega_k t)) \quad (1)$$

where,  $\mathbf{x}_0$  represents the position at the reference epoch  $t_0$  and  $\mathbf{v}$  is the secular velocity. The model also includes, if required, episodic offsets of magnitude  $\mathbf{b}_j$  due to antenna changes at specific epochs  $t_j$  and annual and semi-annual signals  $\mathbf{s}_k$  and  $\mathbf{c}_k$ , with frequencies  $\omega_k$ , to account for seasonal coordinate variations (e.g., due to different loading



effects). Here,  $n_j$  and  $n_p$  represents the number of jumps in the coordinates and the number of Fourier periodic terms modeled, respectively, whereas  $H$  is the Heaviside step function. Also, and to take into account the temporal correlation within each time series, we chose a combination of white noise and Generalised Gauss Markov noise (Langbein, 2004), when appropriate, to provide the stochastic properties of the models. In this case, it was not necessary to model postseismic relaxation or linear trend changes at any site. This indicates that any non-linear displacement of the sites is below the observation noise throughout the observation time span.

### 2.3. Elastic Modeling of Interseismic Surface Deformation Rates

We employ here the method described by Meade and Hager (2005), which relates block motions and fault slip rates to observed interseismic deformation. The method makes use of the analytic solutions given by Okada (1992) for the surface deformation due to an arbitrarily inclined and finite dislocation in a homogeneous elastic half-space. In essence, given a block partition (bounded by faults), fault segments and observations (e.g., GNSS sites), the interseismic deformation rate is explained as the difference between the rotation of the blocks and a yearly coseismic slip deficit. Along each segment of the modeled faults, the rotation of the contiguous blocks, in turn associated with a pair of Euler poles of rotation, results in consistent strike- and tensile-slip rates (for vertical dislocations) or strike- and dip-slip rates (for inclined dislocations). The forward model, besides the definition of geometric properties of each fault segment (e.g., locking depth, inclination, along-strike length), requires only the introduction of the Euler poles of each block. In the inverse problem, the corresponding Euler poles, fault slip rates and some geometric properties of the fault segments can be estimated from the observed surface deformation rates (e.g., GNSS velocities). In general, in order to better solve for the geometric characteristics, known fault slip rates and Euler poles of rotation can be introduced as pseudo observations with appropriate weights. For details on this method and its mathematical formulation refer to Meade and Hager (2005) and L. Mendoza et al. (2015).

In this study, the model consists in the partition of the island in only two blocks, in the SA and SC plates, separated by simplified, finite and piecewise linear fault segments along the main trace of the MF. Here, we use a digitized fault trace mainly adapted from two recent studies (Roy et al., 2019; Sandoval & De Pascale, 2020) but consistent with previous determinations (e.g., Tassone et al., 2005). This approximate fault trace, common to all model versions, is composed of 34 linear segments ranging from 5 to 90 km in length, coarser at the eastern end, and it extends from the Strait of Magellan in the west to the Atlantic Ocean, beyond the east coast of the island (e.g., Figure 8). For each model version we adopt a common locking depth  $D$  and inclination  $\delta$  for all fault segments. In addition, the absolute Euler pole of rotation for the SA plate, referred to a no-net-rotation RF was added as a pseudo observation (model APKIM2005IGN, Drewes, 2009). Similarly, the relative pole of rotation for the SC plate, with respect to fixed SA, was also introduced (model TLP2003, Thomas et al., 2003). Both Euler poles and rotation rates were loosely constrained at a three sigma level. A total of 51 GNSS sites were used to constrain the model parameters, 29 of them located on the SA block and the remaining 22 on the SC block (Figure 3). Three GNSS sites (8, 21, and 37; Figure 1), located more than 150 km away from the main MF trace, were used for control. Furthermore, only the observed horizontal velocities constrain the model parameters during the inversions.

Slip rates estimated in TDF have to be differentiated between rates representing only the MF master fault, the majority, for example, Smalley et al., 2003 ( $6.6 \pm 1.3 \text{ mm a}^{-1}$ ), L. Mendoza et al., 2015 ( $5.9 \pm 0.2 \text{ mm a}^{-1}$ ), Roy et al., 2019 ( $6.4 \pm 0.9 \text{ mm a}^{-1}$ ) or Sandoval and De Pascale 2020 ( $7.8 \pm 1.3 \text{ mm a}^{-1}$ ) and those estimates that describe the effect of the entire MFS including secondary faults, for example, Sandoval and De Pascale 2020, between  $9.1$  and  $12.0 \text{ mm a}^{-1}$  or DeMets et al., 2010 ( $9.6 \pm 1.4 \text{ mm a}^{-1}$ ). However, the contribution of individual secondary structures to the total slip rate accommodated over the MFS is uncertain today. While there is general agreement (among different techniques and within their confidence intervals) regarding the slip rate across MF, the present-day activity of secondary faults such as DF or Hope Fault (e.g., Sandoval & De Pascale, 2020), is controversial and there is hardly any observational basis to constrain the geometry and kinematics (geological slip rate estimates, Euler poles) of possible slip movements along those secondary structures. The limited discriminatory power of our GNSS observations, confined to the surface and a rather narrow section of the plate boundary in addition to suffering from a heterogeneous site distribution, precludes us from resolving the effects of those secondary features in our models with any reasonable degree of confidence. On the other hand, the deformation field sampled by our GNSS network as a whole is expected to be clearly dominated by the slip along MF. For this

reason, our models approximate the surface deformation in TDF by a robust quantification of the interseismic and postseismic movements associated to MF.

A good agreement between geodetic and geological slip rates should be expected (Meade et al., 2013), particularly in this case, where the geodetic observations have been obtained well before the eventual end of the current seismic cycle (associated here to MF), when the next major (periodic) rupture is projected to occur (Dolan & Meade, 2017). At the same time, interseismic locking depths geodetically inferred have been found to be reliable indicators of seismic potential, given their consistency with the thickness of the seismogenic layers found coseismically (Wright et al., 2013). Therefore, and given the high correlation between locking depths and slip rate parameters in our modeling, we prefer to introduce highly constrained geological slip rates. In turn, we obtain reliable and decoupled locking depths, consistent with the corresponding geological observations. However, and although the slip rate estimates made by Roy et al. (2019) and Sandoval and De Pascale (2020) are consistent with each other, within their formal uncertainties, the locking depths needed to make them consistent with the current deformation rates in Tierra del Fuego (i.e., the GNSS velocities) are quite different. Thus, we calculate separate models for each case. Since, we also separate the models according to whether the fault planes are considered vertical or inclined, two alternative models could be associated to each slip rate estimate.

We use Bayesian inference to construct posterior density functions (PDFs) for each of the model parameters (i.e., locking depth  $D$  and inclination  $\delta$ ), applying the Markov chain Monte Carlo method (see, e.g., Spade, 2020), where the sampling is controlled by a Delayed Rejection Adaptive Metropolis algorithm. This method, which has the advantage of providing reliable uncertainties for each estimated parameter, taking into account all available information on the problem, has already been applied to similar geodynamic studies (e.g., Bagnardi & Hooper, 2018; Bruhat, 2019). In particular, we make use of the Python module `pymcmcstat` (Miles, 2019, 2020). For each of the models described before we compute four parallel chains, of  $2 \times 10^4$  samples each, in order to assess the convergence of the PDFs by means of the Gelman–Rubin convergence diagnostic (Gelman & Rubin, 1992). For the elastic modeling we use the Python module `okada-wrapper` (Thomson, 2020) that conveniently wraps the original Fortran implementation made by Y. Okada. The search range for the locking depth  $D$  extends between 1 and 35 km for all models, whereas for those models with non-vertical faults the search range for the inclination  $\delta$  is between 10 and 88.5°, dipping to the south. This search range for the inclination of the modeled dislocations is based on previous results by L. Mendoza et al. (2015) and also on the proposed inclination of  $\sim 80^\circ$ , dipping to the South, made by Tassone et al. (2005) from the interpretation of gravimetric data and structural observations east of Lake Fagnano. The spatial distribution of the epicenters of the low magnitude events occurred in TDF during the last decade (Figure 1), predominantly located south of the MF main trace, also support the consideration of non-vertical dislocations.

#### 2.4. Postseismic Relaxation After the 1949 Tierra Del Fuego Earthquake

The limited number of quantitative observations of the coseismic offset during the 1949 earthquakes, the scarce information on the extent and location of the ruptures (e.g., Abascal & González Bonorino, 2014; Costa et al., 2006; González Bonorino et al., 2011), the lack of agreement on the magnitude of the events (e.g., Di Giacomo et al., 2015, 2018; Jaschek et al., 1982; Lomnitz, 1970; Zamarbide & Castano, 1978), and the absence of any previous model of viscoelastic relaxation in the region make a numerical modeling of the current seismic cycle in Tierra del Fuego a challenge. Indeed, to obtain reliable interseismic locking depths from the elastic modeling, consistent with both the geodetic observations and the adopted geological slip rates, it is necessary to take into account any possible contribution from viscoelastic relaxation associated to past earthquakes (e.g., Tong et al., 2014). That is, a previously computed model available for the study region can be used to correct all observed GNSS velocities prior to the inversion (e.g., Hammond et al., 2011) or, alternatively, an ad-hoc model can be constructed using information about past large events (e.g., magnitudes, coseismic slips, geometry of the surface ruptures). Here, we implement the latter strategy. However, due to the mentioned scarcity of historical information available on the seismic activity in the region, we were forced to make some simplifying assumptions. On the one hand, we adopt three alternative estimates for the moment magnitude of the largest event in 1949:  $M_w = 7.5$  consistent with Lomnitz (1970) and Febrer et al. (2000),  $M_w = 7.7$  consistent with Di Giacomo et al. (2015); Di Giacomo et al., 2018 (ISC-GEM catalog, event `iscgem897093`) and Ammirati et al. (2020) and  $M_w = 7.8$  consistent with Zamarbide and Castano (1978), Jaschek et al. (1982), Pelayo and Wiens (1989), Costa et al. (2006), González Bonorino et al. (2011) and Abascal and González Bonorino (2014). Regardless

of the moment magnitude chosen, for all models we associate with this event a total coseismic surface slip  $s_{EQ} = 6 \pm 0.5$  m, as recently estimated by Roy et al. (2019). Also following Roy et al. (2019), who found evidence that the rupture probably did not reach the Atlantic coast of the island and rather ended up near Malengüena Hill (MH, Figure 1), we assign this common displacement  $s_{EQ}$  to all fault segments located to the west of this place, essentially fixing the eastern end of the simulated coseismic surface rupture. On the other hand, from the estimated parameters obtained after the elastic modeling, it is possible to compute the downdip width  $W$  of the faulting plane as

$$W = D \text{ (vertical fault)} \quad \text{or} \quad W = \frac{D}{\sin\delta} \text{ (inclined fault)} \quad (2)$$

the released seismic moment can be derived from the adopted moment magnitude  $M_w$  as

$$M_0 = 10^{\frac{3}{2}M_w + 9.1} \quad (3)$$

from its definition (Kanamori, 1983). In turn, from Equation 2 to 3 we can now estimate a length for the rupture that occurred during this 1949 earthquake as

$$L_{EQ} = \frac{M_0}{\mu s_{EQ} W} \quad (4)$$

where  $\mu = 30$  GPa is the shear modulus (Hanks & Kanamori, 1979). Here, we make use of the adopted coseismic slip  $s_{EQ}$  and the downdip width  $W$  estimates inferred from the present-day GNSS observations. Therefore, and for each of the models, it is now possible to locate the western end of the simulated coseismic surface rupture, with the help of  $L_{EQ}$ , using here exactly the same approximate fault trace previously adopted for the MF.

In order to quantify the coseismic deformation occurred in 1949 we apply here the software Relax (see Barbot, 2014; Barbot & Fialko, 2010a; Barbot & Fialko, 2010b), which uses an equivalent body-force representation of the processes. The software output is further processed using the Generic Mapping Tools (Wessel et al., 2019). Letting the simulation evolve during more than 60 years we also estimate the rates of postseismic deformation expected at the mean epoch of observation  $t_{GNSS}$  of the geodetic data. For this purpose we define an elastic layer with thickness  $H = 45$  km, and density  $\rho = 2810$  kg m<sup>-3</sup>, adopting the mean depth of the Lithosphere-Asthenosphere boundary and the crust density provided by the global model LithRef18 (Afonso et al., 2019). This layer is overlaid on a viscoelastic half-space with an effective viscosity  $\eta = 5 \times 10^{18}$  Pa s using the average of the two effective viscosity estimates obtained by Lange et al. (2014). The model is setup within a Fourier domain grid of  $512 \times 512 \times 512$  cubic cells, with edges of 1 km in length. The lower half of the grid is exclusively employed to set up the body-force images. The two effective viscosity estimates obtained by Lange et al. (2014), and constrained by observed uplifts, were obtained when modeling a rapid ongoing glacial isostatic adjustment (GIA) process in continental Patagonia. This apparently low viscosity, in fact compatible with best-fit effective mantle viscosities found for various other seismic relaxation scenarios (e.g., in Alaska, in Tibet, in Montana, see review by Bürgmann & Dresen, 2008), proved to be also adequate for modeling the relaxation process in Tierra del Fuego, particularly the observed vertical deformation rates (see results and discussion).

Within the rather simple rheological assumptions described above, and for each of the models, we use the corresponding downdip width  $W$  of the faulting plane, fault inclination  $\delta$ , and the subset of fault segments that accommodates the estimated rupture length  $L_{EQ}$ , to simulate the coseismic and left-lateral slip of magnitude  $s_{EQ}$ , source of the seismic event in 1949. Then, the relaxation velocity field obtained for the epoch  $t_{GNSS}$  can be used to correct the horizontal deformation rates observed with GNSS. In turn, these corrected observations can be inverted again, resulting in new estimates of  $W$ ,  $\delta$  and  $L_{EQ}$ . Only three iteration of this alternate procedure are required to obtain a final set of estimated parameters that are consistent, within the formal uncertainties, with the a priori long-term (i.e., geological) slip rates, the seismic moment magnitudes adopted and the present-day GNSS observations. In total 12 models were adjusted, according to whether the fault planes were considered vertical or inclined (models' names beginning with V or I, respectively), whether the geological slip rate was adopted from Roy et al. (2019) or from Sandoval and De Pascale (2020) (models' names with R or S, respectively) and according to each of the alternative moment magnitudes considered (models' names ending with 7.5, 7.7 or 7.8, respectively). All the calculations described in this section and in the previous one (i.e., the elastic block modeling and the correction



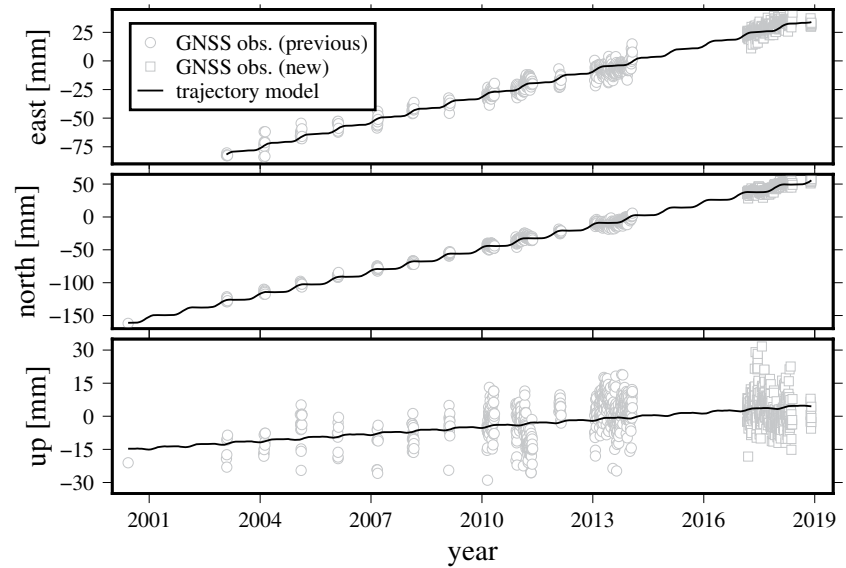


**Figure 2.** Example of daily Global Navigation Satellite System solutions and trajectory models: site 48, materialized by a bronze bolt in bedrock in the geothermal area of Río Valdez (Capaccioni et al., 2013), 10 kilometers south of Lake Fagnano (Figure 1).

for viscoelastic relaxation) can be reproduced with the help of 12 interactive Jupyter notebooks (one for each model), a common Python module and a simple Bash script, all of them provided as Supporting Information S1.

### 3. Results and Discussion

#### 3.1. Trajectory Models and Deformation Rates

In practice, only eight semi-permanent or continuously operating stations require the incorporation of yearly and half-yearly periodic terms into the trajectory models. Among these cases, some of the largest amplitudes correspond to site 48, south of Lake Fagnano (Figure 1), with annual amplitudes of  $1.6 \pm 0.7$ ,  $2.9 \pm 0.4$  and  $1.7 \pm 0.9$  mm, in the east, north and vertical components, respectively, whereas the half-annual amplitudes amount to  $0.8 \pm 0.4$ ,  $0.7 \pm 0.3$  and  $1.2 \pm 0.6$  mm, in the east, north and vertical components, respectively. These parameters may account for displacements due to seasonal variations in hydrologic load due to rainfall in summer, snowfall in winter or seasonal lake level variations of LF (Richter et al., 2010). As expected the vertical components of the daily GNSS solutions show the highest dispersion (e.g., Figure 2). Nevertheless, the precision (i.e., repeatability) of the daily coordinates is on par with our previous analysis using a double-difference GNSS method. The geographic consistency of the estimated horizontal rates is also comparable to the results obtained with differential methods (L. Mendoza et al., 2011; L. Mendoza et al., 2015), although here the GNSS observations of each site are processed independently. That is, they are only indirectly correlated through the common orbital products and not by the relative geometry of a network during simultaneous observing sessions, along many campaigns. All this provides evidence of the high quality and consistency of the orbital products used. Of course, the reliability of the deformation rate estimates (Table 1, Figure 3) clearly benefits from the incorporation of more GNSS observations with respect to our previous works, particularly the vertical components. The added observations allow us to extend the time frame of the geodetic monitoring, and to improve the spatial distribution of the data by obtaining estimators for several episodic GNSS sites previously not yet incorporated because of the limited number of occupations available at that time. In fact, here we employ 54 regional GNSS sites, while in previous works we employed only 29 and 48 sites (L. Mendoza et al., 2011; L. Mendoza et al., 2015, respectively). As mentioned, the resulting position time series and the corresponding deformation rate estimates for each site are independent from each other. Also, the estimated vertical coordinates and rates are absolute and refer to a common, stable and global origin (the IGS14 RF, as materialized in satellite orbits and clocks for 24 years), not being distorted, for example, by defects in the orientation (or the orientation rate) of any regional network.

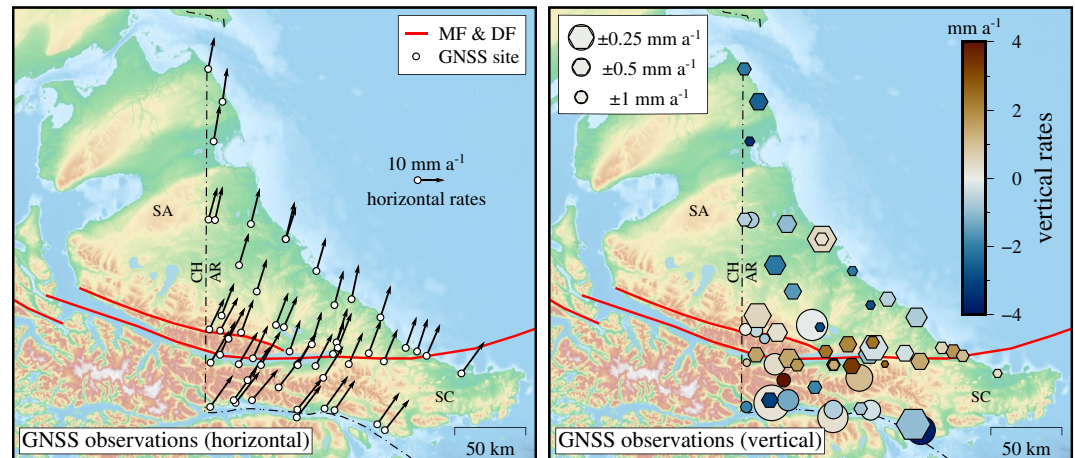


**Figure 3.** Present-day horizontal and vertical deformation rates observed in Tierra del Fuego and derived from a Global Navigation Satellite System data set spanning 24 years. The horizontal velocities (in the left panel), mostly oriented to the north, indicate the concurrent motion of the South American and Scotia blocks in a non-net-rotation, global reference frame, in this case the IGS14 (Rebischung & Schmid, 2016). Right panel: circles indicate benchmarks built on bedrock while hexagons indicate benchmarks (concrete pillars) located on sedimentary deposits. The narrow deformation belt along the tectonic boundary between the SA and SC plates, about 20–50 km wide (L. Mendoza et al., 2011; Sandoval & De Pascale, 2020), is visible as a slight change in the overall direction of these horizontal velocities and even more evident in the elongated E-W uplift pattern (in the right panel), closely aligned with the Magallanes-Fagnano Fault. Acronyms: AR (Argentina), CH (Chile), DF (Deseado Fault).

Before discussing any model, it is worth noting the clear pattern of active uplift that can be observed along the MF sections in Tierra del Fuego (Figure 3, right panel), limited to the very narrow, approximately 20–50 km wide, plate boundary deformation zone (see L. Mendoza et al., 2011; Sandoval & De Pascale, 2020). Although at each site local processes, observation errors, and modeling biases are undoubtedly responsible for some dispersion in the observed uplift rates, this localized pattern contrasts sharply with the subsidence observed at most GNSS sites outside this narrow band, both south and north of the MF main trace. At first glance, this appears to be in agreement with the evidence of rapid tectonic uplift suggested by Perucca et al. (2015) studying the features of several river courses, east of Lake Fagnano (e.g., the ratio between uplift rates and erosion rates, truncated meanders, abandoned fluvial valleys). Of course, other processes could be involved (e.g., glacial isostatic rebound, discussed below).

### 3.2. Modeling Parameters and Inferred Deformation

The 12 models implemented result in substantially different parameter estimates (Table 2), which are particularly influenced by the geological slip rate adopted and, to a lesser extent, by the inclination of the fault planes and the moment magnitudes. For all models, the mean residual results in  $\sim 0.7 \text{ mm a}^{-1}$ , whereas the mean uncertainty of the observations is  $\sim 0.5 \text{ mm a}^{-1}$  (Table 1). While all models are capable of accommodating the observed horizontal GNSS velocities, those models with a slip rate  $\dot{s}$  adopted from Roy et al. (2019) produce both the minimum misfit and the narrowest confidence intervals (Figures 4 and 5), given the statistical properties of the PDFs obtained for each parameter. Models VR7.5 and IR7.5 produce slightly smaller horizontal residuals than models VR7.7 and IR7.7. However, models VR7.7 and IR7.7 better reproduce the vertical signal observed at the northern sites (see below). Models that adopt the largest of the moment magnitudes (i.e., 7.8) produce the largest horizontal residuals. As mentioned above, the slip rate estimates made by Roy et al. (2019) and Sandoval and De Pascale (2020) are in fact consistent with each other, within their uncertainties. However, models VR7.5, VR7.7 and VR7.8 result in interseismic locking depths that are  $\sim 65\%$  smaller than those corresponding to models VS7.5, VS7.7, and VS7.8, respectively, whereas models IR7.5, IR7.7 and IR7.8 result in interseismic locking depths that are  $\sim 55\%$  smaller than those corresponding to models IS7.5, IS7.7, and IS7.8, respectively (Table 2). Conversely, the comparisons of the same pairs of models, but with respect to the surface rupture length estimates, result in an increase of 65% and 55%, respectively (Table 2). This in turn leads to significantly different scenarios when modeling the coseismic deformation and the subsequent time-dependent relaxation (see below). Indeed,

**Table 1**  
*Interseismic Deformation Rates Observed at Regional GNSS Sites*

Site #	Lat. [deg]	Long. [deg]	$v_e$ [mm a <sup>-1</sup> ]	Daily sol. $e$	$v_n$ [mm a <sup>-1</sup> ]	Daily sol. $n$	$v_u$ [mm a <sup>-1</sup> ]	Daily sol. $u$	$\Delta T$ [years]
1 <sup>a</sup>	-54.840	-68.304	8.92 ± 0.09	5,694	11.53 ± 0.03	5,694	0.24 ± 0.13	5,675	20.0
2 <sup>a</sup>	-54.378	-68.472	6.58 ± 0.50	11	12.29 ± 1.65	11	-0.47 ± 1.02	11	2.0
3 <sup>a</sup>	-54.695	-68.171	8.40 ± 0.55	17	12.42 ± 0.70	17	4.32 ± 0.91	17	3.9
4 <sup>a</sup>	-54.583	-68.578	6.94 ± 0.77	15	11.81 ± 0.43	15	0.81 ± 2.95	15	3.9
5	-54.823	-68.324	8.61 ± 0.17	35	11.85 ± 0.20	35	-3.05 ± 0.61	39	24.0
6 <sup>a</sup>	-54.886	-67.214	7.64 ± 0.33	540	11.10 ± 0.17	540	-0.27 ± 0.42	537	7.7
7 <sup>a</sup>	-54.341	-67.859	4.56 ± 0.06	485	11.88 ± 0.12	485	-0.06 ± 0.17	490	8.2
8	-52.881	-68.447	1.77 ± 0.28	7	12.54 ± 0.36	7	-2.48 ± 0.47	7	3.0
9	-54.511	-66.306	3.94 ± 0.15	26	12.07 ± 0.27	26	1.78 ± 0.72	27	6.9
10	-53.955	-68.265	3.54 ± 0.28	65	11.78 ± 0.13	65	-2.10 ± 0.36	65	18.2
11 <sup>a</sup>	-54.822	-68.122	9.52 ± 0.10	24	11.26 ± 0.21	24	-1.31 ± 0.37	25	7.8
12	-54.528	-67.231	4.03 ± 0.62	45	11.97 ± 0.34	45	-1.01 ± 0.36	48	16.2
13	-54.593	-67.058	5.19 ± 0.74	20	11.62 ± 0.61	20	2.65 ± 2.96	20	7.0
14	-54.556	-68.113	5.55 ± 0.20	42	12.15 ± 0.04	42	1.49 ± 0.38	40	10.9
15	-54.523	-66.838	4.50 ± 0.40	33	12.13 ± 0.23	33	-0.30 ± 0.50	34	9.0
16	-54.466	-67.464	3.61 ± 0.17	35	11.95 ± 0.14	35	2.04 ± 0.54	37	10.0
17	-53.687	-68.134	3.30 ± 1.23	12	13.21 ± 0.50	12	-1.02 ± 0.44	12	6.1
18	-54.454	-67.191	4.00 ± 0.35	28	12.58 ± 0.58	28	2.35 ± 0.94	28	4.9
19	-54.126	-68.071	3.70 ± 0.39	22	11.96 ± 0.18	22	-1.59 ± 0.55	24	18.2
20	-54.876	-67.324	8.58 ± 0.27	37	11.93 ± 0.08	37	-0.80 ± 0.91	37	21.7
21	-52.662	-68.605	2.25 ± 1.22	17	11.69 ± 0.09	17	-2.06 ± 0.85	17	4.9
22	-54.175	-67.027	2.70 ± 0.33	847	12.77 ± 0.47	847	-0.59 ± 0.63	863	8.0
23	-54.575	-66.671	5.03 ± 0.12	39	11.81 ± 0.24	39	1.42 ± 0.48	39	8.0
24	-54.605	-67.423	6.25 ± 0.28	33	11.90 ± 0.18	33	3.34 ± 0.55	34	10.0
25 <sup>a</sup>	-54.865	-68.582	8.34 ± 0.62	15	11.69 ± 0.12	15	-1.92 ± 1.31	15	5.8
26	-54.652	-65.819	8.55 ± 0.82	12	11.70 ± 0.36	12	0.37 ± 1.95	12	2.9
27	-54.540	-66.201	5.00 ± 0.20	23	11.67 ± 0.51	23	1.13 ± 0.99	26	6.9
28	-54.489	-66.431	3.98 ± 0.33	91	11.41 ± 0.36	91	0.56 ± 0.96	90	5.9
29	-54.975	-66.745	8.19 ± 0.30	30	11.66 ± 0.19	30	-1.00 ± 0.14	34	24.0
30	-54.282	-68.457	4.65 ± 0.18	185	11.96 ± 0.14	185	0.53 ± 0.22	184	15.5
31	-54.599	-68.024	7.25 ± 0.49	31	12.41 ± 0.24	31	1.74 ± 0.91	31	9.0
32	-54.533	-68.475	5.67 ± 0.16	28	12.36 ± 0.13	28	1.53 ± 0.62	25	10.9
33	-54.213	-67.216	3.33 ± 0.28	24	12.64 ± 0.61	24	-2.81 ± 1.77	28	16.2
34	-54.595	-67.625	6.99 ± 0.46	34	11.57 ± 0.45	34	4.34 ± 0.88	34	9.0
35	-54.599	-67.619	6.87 ± 0.66	14	11.71 ± 1.15	14	1.37 ± 1.30	14	1.9
36 <sup>a</sup>	-54.932	-67.630	9.02 ± 0.10	1,476	11.78 ± 0.16	1,476	0.31 ± 0.18	1,463	5.2
37	-53.144	-68.544	2.28 ± 0.54	10	13.39 ± 0.23	10	-3.50 ± 1.67	10	6.1
38	-53.786	-67.751	3.31 ± 0.38	704	13.80 ± 0.52	704	0.34 ± 0.86	704	2.0
39	-54.741	-67.829	9.07 ± 0.61	43	11.80 ± 0.33	43	-1.89 ± 0.83	44	16.2
40	-54.390	-68.242	4.52 ± 0.33	42	12.15 ± 0.21	42	0.30 ± 0.40	44	19.1
41	-53.785	-67.751	3.83 ± 0.15	6,411	11.94 ± 0.06	6,411	0.49 ± 0.19	6,415	19.0
42	-54.512	-67.710	4.00 ± 0.41	31	11.67 ± 0.26	31	2.35 ± 0.85	31	8.1



**Table 1**  
*Continued*

Site #	Lat. [deg]	Long. [deg]	$v_e$ [mm a <sup>-1</sup> ]	Daily sol. $e$	$v_n$ [mm a <sup>-1</sup> ]	Daily sol. $n$	$v_u$ [mm a <sup>-1</sup> ]	Daily sol. $u$	$\Delta T$ [years]
43 <sup>a</sup>	-54.430	-68.382	6.12 ± 1.14	15	11.43 ± 0.78	15	-0.75 ± 1.73	15	3.9
44	-53.658	-68.602	3.26 ± 0.29	16	11.86 ± 0.42	16	-0.58 ± 0.77	16	8.0
45 <sup>a</sup>	-53.661	-68.529	2.78 ± 0.11	10	12.38 ± 0.08	10	-0.73 ± 0.68	10	4.8
46	-54.293	-66.710	3.85 ± 0.27	29	11.78 ± 0.21	29	-0.69 ± 0.36	33	18.1
47 <sup>a</sup>	-55.012	-66.660	8.98 ± 0.05	8	11.27 ± 0.08	8	-3.82 ± 0.20	11	5.8
48 <sup>a</sup>	-54.680	-67.340	7.44 ± 0.13	1,079	11.69 ± 0.07	1,079	1.08 ± 0.23	1,078	18.5
49 <sup>a</sup>	-54.593	-68.268	6.98 ± 0.10	300	11.86 ± 0.05	300	0.40 ± 0.36	300	15.4
50 <sup>a</sup>	-54.370	-68.592	5.56 ± 0.84	19	11.49 ± 0.97	19	0.10 ± 1.16	19	2.9
51	-54.488	-67.178	5.07 ± 0.13	788	12.87 ± 0.26	788	-0.28 ± 0.21	795	8.7
52	-53.993	-67.414	3.53 ± 1.08	23	12.27 ± 0.49	23	-2.08 ± 1.55	20	16.2
53 <sup>a</sup>	-54.882	-67.625	9.19 ± 0.17	21	11.47 ± 0.13	21	-0.65 ± 0.48	21	8.7
54	-54.356	-67.772	4.94 ± 0.41	27	11.41 ± 0.75	27	-2.87 ± 1.71	28	16.2

*Note.* Lat., Long.: site latitude and longitude, respectively;  $v_e$ ,  $v_n$ ,  $v_u$ : east, north and vertical velocities, respectively; sol.: number of daily GNSS solutions on each component, which are independent due to the outlier rejection scheme implemented during time series analysis;  $\Delta T$ : time span between the earliest and latest daily solution obtained for each site.

<sup>a</sup>Indicates benchmarks built on bedrock, all other benchmarks (concrete pillars) are located on sedimentary deposits (also indicated in Figure 3, right panel).

models IS7.5, IS7.7, IS7.8, and particularly VS7.5, VS7.7, and VS7.8, would imply an almost complete coseismic rupture of the crust during the seismic event in 1949, as well as an interseismic locking of the fault planes that extends almost to the upper mantle, if a crustal thickness of 35 km from the global LithRef18 model (Afonso et al., 2019) is adopted here. We reach the same conclusion if we instead adopt the regional estimates made by Buffoni et al. (2019) or Ammirati et al. (2020) that indicate a crustal thickness ranging from 25 to 35 km or from 25 to 30 km, respectively. On the other hand, the results of models VR7.5, VR7.7, VR7.8, and particularly IR7.5, IR7.7, and IR7.8, point more clearly to intracrustal processes and are more consistent with modern seismic records in Tierra del Fuego that account for shallow seismic events along MF (Ammirati et al., 2020). In the same sense, Buffoni et al. (2009) observed that the hypocentral depths, for half of the low magnitude events in the region, do not exceed 10 km. Also, models IR7.5, IR7.7 and IR7.8 are more consistent with the hypocentral depth of ~13 km attributed by Jäschek et al. (1982) to the largest of the 1949 earthquakes, and also with the most recent estimate of ~10 km (Bondár et al., 2015). Furthermore, the results of these models are the most consistent with the estimates made by Wright et al. (2013) for both the seismogenic thickness ( $14 \pm 5$  km) and the interseismic locking depths ( $14 \pm 7$  km) derived globally from geodetic solutions for earthquakes and interseismic geodetic inversions (also see Wright, 2016). In general, our models result in inferred locking depths larger than our previous estimates, which ranged between  $10^{+5}_{-4}$  and  $15^{+9}_{-7}$  km (see L. Mendoza et al., 2015). These differences can be attributed primarily to the viscoelastic relaxation affecting each of the GNSS sites, as the corresponding slip rate estimates, which ranged between 5.4 and 6.8 mm a<sup>-1</sup>, are consistent with the long-term slip rate we adopt here for half of the models (i.e., Roy et al.'s estimate). That is, by not taking into account the postseismic relaxation into the modeling, in L. Mendoza et al. (2015) we underestimated by 25%–50% the width of those fault planes that could dislocate in a complete coseismic rupture.

However, none of the models is able to approximate the horizontal velocity observed in three particular sites (i.e., sites 2, 43 and 50 indicated in Figures 4 and 5) all of them located near the DF (see Figure 1). Although the spatial distribution of our data cannot constrain the movement of an additional (third) block, delimited by MF and DF, nor reliably constrain an interseismic locking depth for DF, the geodetic observations do indicate the possibility that some movement is being accommodated through it. In this respect, evidence of active movement during the Quaternary has already been associated with the DF deformation zone (Klepeis, 1994), although its long-term velocity remains unknown. Sandoval and De Pascale (2020) found evidence of very recent seismic ruptures along the DF fault trace, post 1680 according to field observations. The deformation field sampled by our GNSS network is certainly dominated by the effects originating along MF, even at the sites to the north of DF.

**Table 2**  
Summary of the Parameters of the Calibrated Models

Model	Input parameters		Output parameters			Model misfit
	$\dot{s}^a$ [mm a <sup>-1</sup> ]	$M_w^b$ (1949 EQ)	$\delta$ [deg]	$D$ [km]	$L_{EQ}$ [km]	$\sum r^2$ [mm <sup>2</sup> a <sup>-2</sup> ]
VR7.5	6.4	7.5	90°	18.1 ± 2.5	71 ± 12	42.9
VR7.7	6.4	7.7	90°	20.4 ± 3.0	125 ± 22	43.5
VR7.8	6.4	7.8	90°	20.4 ± 2.9	177 ± 31	45.5
VS7.5	7.8	7.5	90°	28.4 ± 3.0	45 ± 6	48.8
VS7.7	7.8	7.7	90°	29.7 ± 2.9	85 ± 11	48.1
VS7.8	7.8	7.8	90°	30.6 ± 2.7	116 ± 15	48.3
IR7.5	6.4	7.5	63.6 ± 4.1	13.2 ± 2.4	88 ± 20	43.2
IR7.7	6.4	7.7	63.4 ± 4.1	14.8 ± 2.7	156 ± 36	43.5
IR7.8	6.4	7.8	62.2 ± 4.4	14.4 ± 2.7	225 ± 53	45.4
IS7.5	7.8	7.5	60.9 ± 4.4	24.2 ± 3.2	46 ± 8	49.9
IS7.7	7.8	7.7	60.9 ± 4.2	25.8 ± 3.2	86 ± 14	48.6
IS7.8	7.8	7.8	61.0 ± 4.2	26.3 ± 3.2	119 ± 19	49.7

Note.  $D$ : interseismic locking depth;  $\delta$ : fault's inclination (vertical or dipping to the south);  $L_{EQ}$ : surface rupture length;  $r^2$ : modeling squared residuals;  $M_w$ : seismic moment magnitude;  $\dot{s}$ : slip rate across MF; EQ: earthquake.

<sup>a</sup>Slip rate  $\dot{s}$  is not estimated,  $\dot{s} = 6.4$  mm a<sup>-1</sup> adopted from Roy et al. (2019) and  $\dot{s} = 7.8$  mm a<sup>-1</sup> adopted from Sandoval and De Pascale (2020). <sup>b</sup>Magnitude  $M_w$  is not estimated,  $M_w = 7.5$  consistent with Lomnitz (1970) and Febrer et al. (2000),  $M_w = 7.7$  consistent with Di Giacomo et al. (2015); Di Giacomo et al. (2018) and Ammirati et al. (2020) and  $M_w = 7.8$  consistent with Zamarbide and Castano (1978), Jaschek et al. (1982), Pelayo and Wiens (1989), Costa et al. (2006), González Bonorino et al. (2011) and Abascal and Gonzáles Bonorino (2014). <sup>c</sup>Inclination  $\delta$  is imposed (i.e., vertical dislocations).

Restricting the modeling of the TDF deformation field to the MF effect is, of course, an approximation but a reasonable and admissible one. On the other hand, nine of the 12 models overestimate the fault-parallel velocity in the three GNSS sites, which do not constrain the modeling parameters, and are located far north of the MF main trace (i.e., sites 8, 21 and 37 indicated in Figures 4 and 5). This velocity step, with a magnitude of  $\sim 1$  mm a<sup>-1</sup>, could be attributed to some component of oblique-slip accommodated across the normal faults bounding the IB–SSB graben (Figure 1) and other extensional structures proposed in the northern part of the island (e.g., Diraison et al., 1997; Menichetti et al., 2008; De Pascale, 2021). The same observed signal has been attributed to fuzzy (i.e., distributed) deformation related to the close triple junction between AN, SA and SC plates (Smalley et al., 2003). In any event, for this reason we chose to not consider these three observation sites in the geodetic inversion for the model parameters.

The difficulty of all models to accurately reproduce the vertical GNSS velocities, that do not constrain the modeling parameters, is quite evident (Figures 6 and 7). However, models with inclined fault planes dipping to the south reproduce to some degree the vertical deformation observed along the fault trace, within the deformation zone. Furthermore, all non-vertical models result in similar estimates for the inclination  $\delta$ , regardless of the adopted slip rate, which are also consistent with our previous and purely elastic modeling (L. Mendoza et al., 2015). Mechanical models involving dislocations with similar inclinations (i.e., between 60° and 70°) have been proposed for segments of the San Andreas Fault system, for example, in order to make them more consistent with the observed uplift patterns (Fattaruso et al., 2014). Moreover, the estimated inclinations obtained by our modeling are fully consistent with recent moment tensor solutions obtained for the  $M_b = 4.2$  event occurred in TDF on 6 November 2009, at 3:37:41.8 UTC (ISC catalog ID 14 193 162, Storchak et al., 2020). These solutions point to a rupture plane dipping of about 70° to the south, with the epicenter clearly associated to the MF, and located near the mouth of AS (Figure 3.14 and Table 3.10 in Bollini, 2021). Nonetheless, all models underestimate the observed uplift over the MF trace, particularly those models with vertical fault planes, all resulting in slightly higher residuals at the southern sites, in the SC block. The two-block model employed here, with connected piecewise linear fault segments, cannot accurately reproduce many of the structures observed along this transform system, neither pop-ups, pressure ridges and uplifted slivers of crust nor the elongated pull-apart basins (Menichetti et al., 2008). However, the uplift and the subsidence expected from the models along the fault

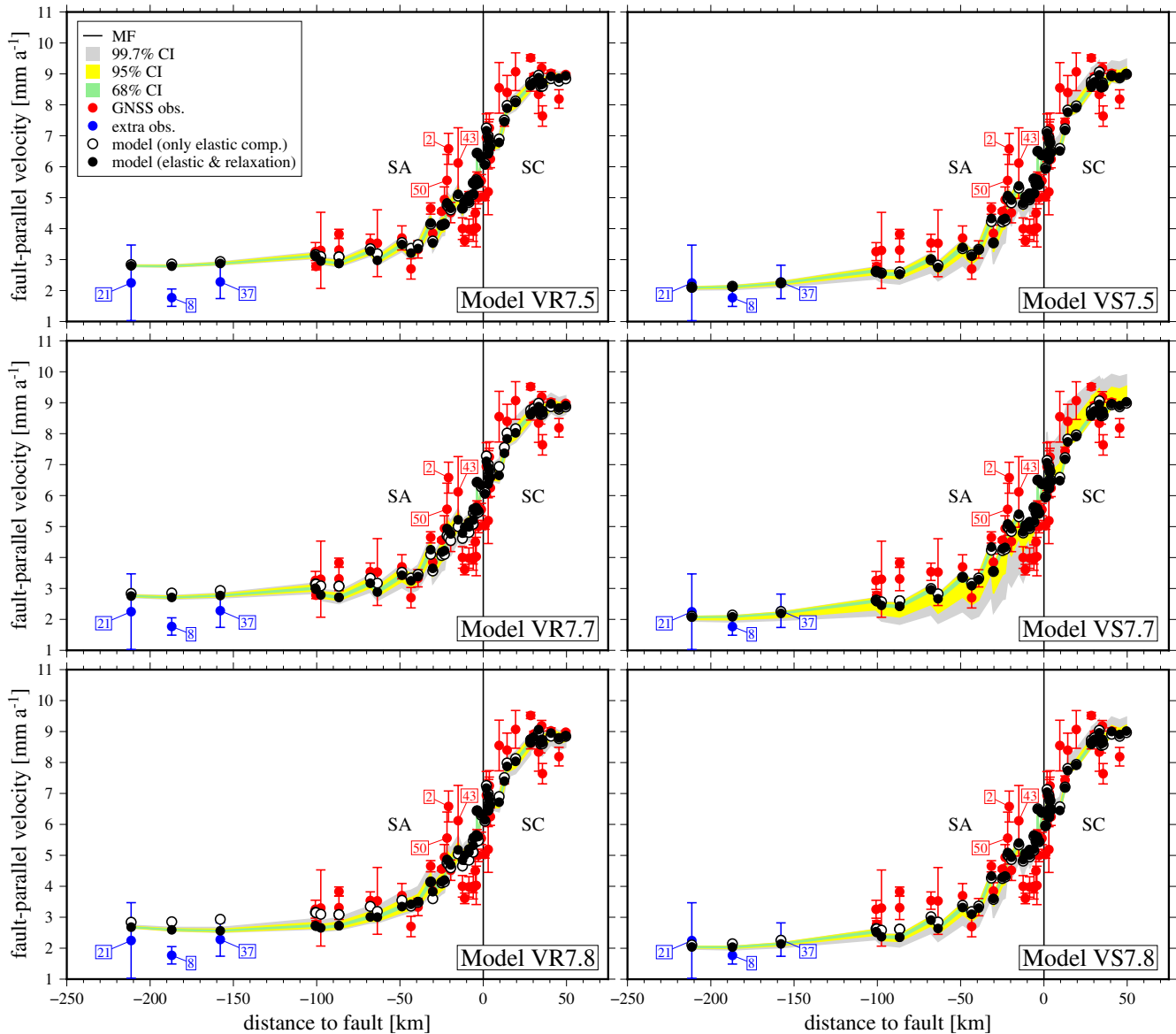


**Figure 4.** Observed and modeled horizontal, fault-parallel velocities across the Magallanes-Fagnano Fault (MF), in Tierra del Fuego, and confidence intervals of the predictions, taking into account the uncertainties of the calibrated model parameters. Models assuming vertical fault segments are shown here. The numbered observations correspond to entries in Table 1 and GNSS sites plotted in Figure 1, red numbers indicate observations suggesting movement along the Deseado Fault, blue numbers indicate observations evidencing lateral movement across extensional structures north of the MF and/or distributed deformation. This figure is supplemented by Figure S1 in Supporting Information S2, which amplifies the narrow deformation belt along the tectonic boundary. Acronyms: SA (South American block/plate), SC (Scotia block/plate).

segments result from a rough elastic representation of those compressional and extensional structures. Indeed, the varying orientation of the modeled fault segments, with respect to the estimated Euler poles of rotation of each block, is responsible for the dip-slip rate component (either normal or reverse) that, in turn, produces the vertical deformation (Meade & Hager, 2005). That said, it is worth noting that the order of magnitude of the observed and the modeled vertical rates in this narrow deformation belt are quite similar, a remarkable coincidence since only the horizontal velocities constrain the calibration of the model parameters.

The fault section sampled by our near-fault GNSS sites corresponds to a large extent with the valley occupied by Lake Fagnano and almost all prominent positive residuals concentrate within this area. During the Last Glacial Maximum (LGM, ~20 ka ago) this valley was completely occupied by an ice lobe (e.g., Lozano et al., 2021; Rabassa et al., 2011; Waldmann, Ariztegui, et al., 2010). This lobe formed part of the extensive glacial system that



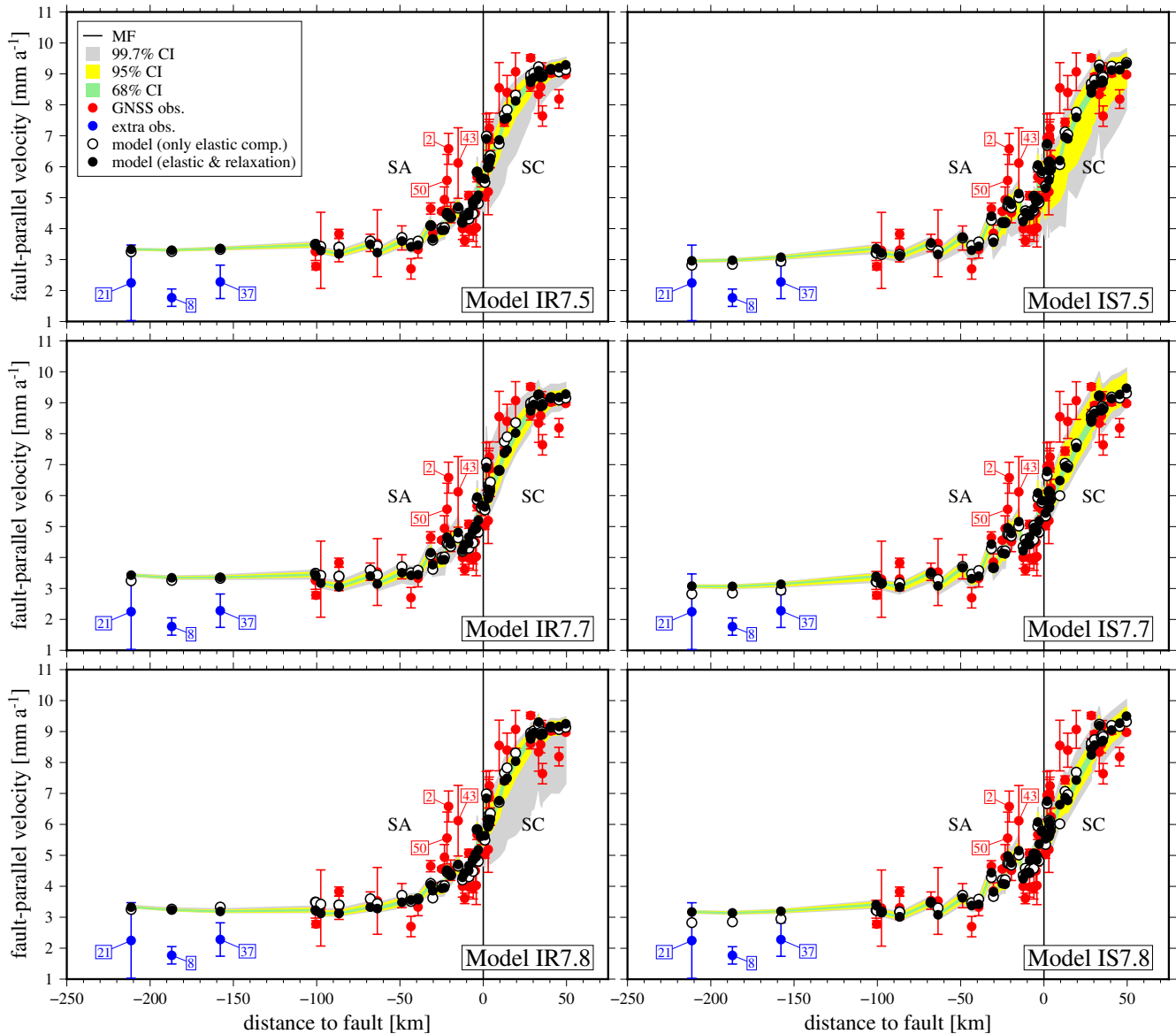


**Figure 5.** Observed and modeled horizontal, fault-parallel velocities across the Magallanes-Fagnano Fault (MF), in Tierra del Fuego, and confidence intervals of the predictions, taking into account the uncertainties of the calibrated model parameters. Models assuming inclined fault segments are shown here. The numbered observations correspond to entries in Table 1 and GNSS sites plotted in Figure 1, red numbers indicate observations suggesting movement along the Deseado Fault, blue numbers indicate observations evidencing lateral movement across extensional structures north of the MF and/or distributed deformation. This figure is supplemented by Figure S2 in Supporting Information S2, which amplifies the narrow deformation belt along the tectonic boundary. Acronyms: SA (South American block/plate), SC (Scotia block/plate).

extended from the Cordillera Darwin into the valleys today occupied by the Beagle Channel and the branches of the Strait of Magellan (e.g., McCulloch et al., 2005). The geographical coincidence of the GNSS sites of maximum residual uplift (Figure 3) with past ice cover may motivate the consideration of ongoing GIA to post-LGM ice-load changes as an explanation of this localized, intense residual deformation signal. However, several caveats make such an interpretation anything but straightforward. First, the striking alignment of observed uplift with the plate boundary raises the question why no uplift of similar magnitude is detected in the neighboring, formerly glaciated valleys (e.g., along Beagle Channel). Second, a significant E-W uplift gradient is expected from GIA, with maximum uplift close to the glaciation center where the glaciers were thicker and deglaciation occurred later. However, such an E-W uplift gradient is not observed along the LF valley. Third, a solid statement about a present-day detectability of GIA-driven deformation in the area covered by our network would require detailed

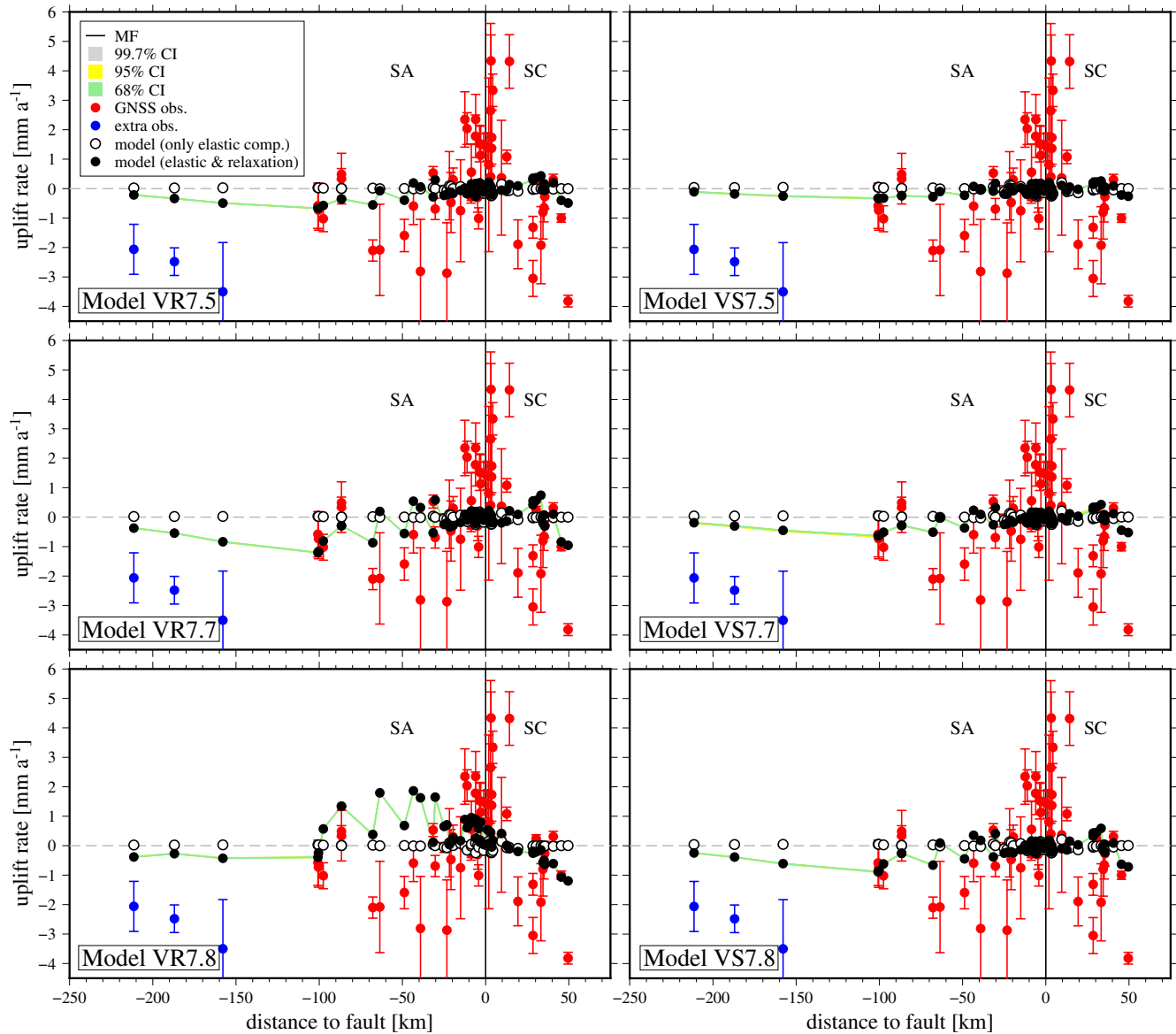


**Figure 6.** Fault-perpendicular profiles of observed and modeled vertical deformation rates across the Magallanes-Fagnano Fault (MF), in Tierra del Fuego, and confidence intervals of the predictions (barely noticeable), taking into account the uncertainties of the calibrated model parameters. Models assuming vertical fault segments are shown here. The narrow deformation belt along the tectonic boundary between the South American and Scotia plates, about 20–50 km wide, is evident in the uplift pattern close to the MF. This figure is supplemented by Figure S3 in Supporting Information S2, which amplifies the narrow deformation belt along the tectonic boundary.

knowledge of both the solid-earth rheology and the regional ice-load history. The viscoelastic earth model derived by Lange et al. (2014) around the Southern Patagonian Icefield, the nearest observationally constrained earth model, implies so fast a relaxation that post-LGM loading effects would have faded long ago (Ivins & James, 2004). A dedicated GIA modeling would be required to estimate present-day magnitudes of GIA effects in Tierra del Fuego, which is beyond the scope of the present work.

On the other hand, several models are able to fairly reproduce the vertical velocity observed at the five sites in the SA block, about ~100 km north of the MF trace, and whose profile shows a step of ~1 mm a<sup>-1</sup> (e.g., models VR7.7 and IR7.7, Figures 6 and 7). This match is only possible if the viscoelastic relaxation is taken into account, since the elastic component of none of the models predicts any vertical deformation rate more than ~30 km away from the fault sections. Further away from the fault, some models reproduce the observed velocity pattern shown at the three additional sites, located more than 150 km north of the MF trace, also in the SA block (e.g., models

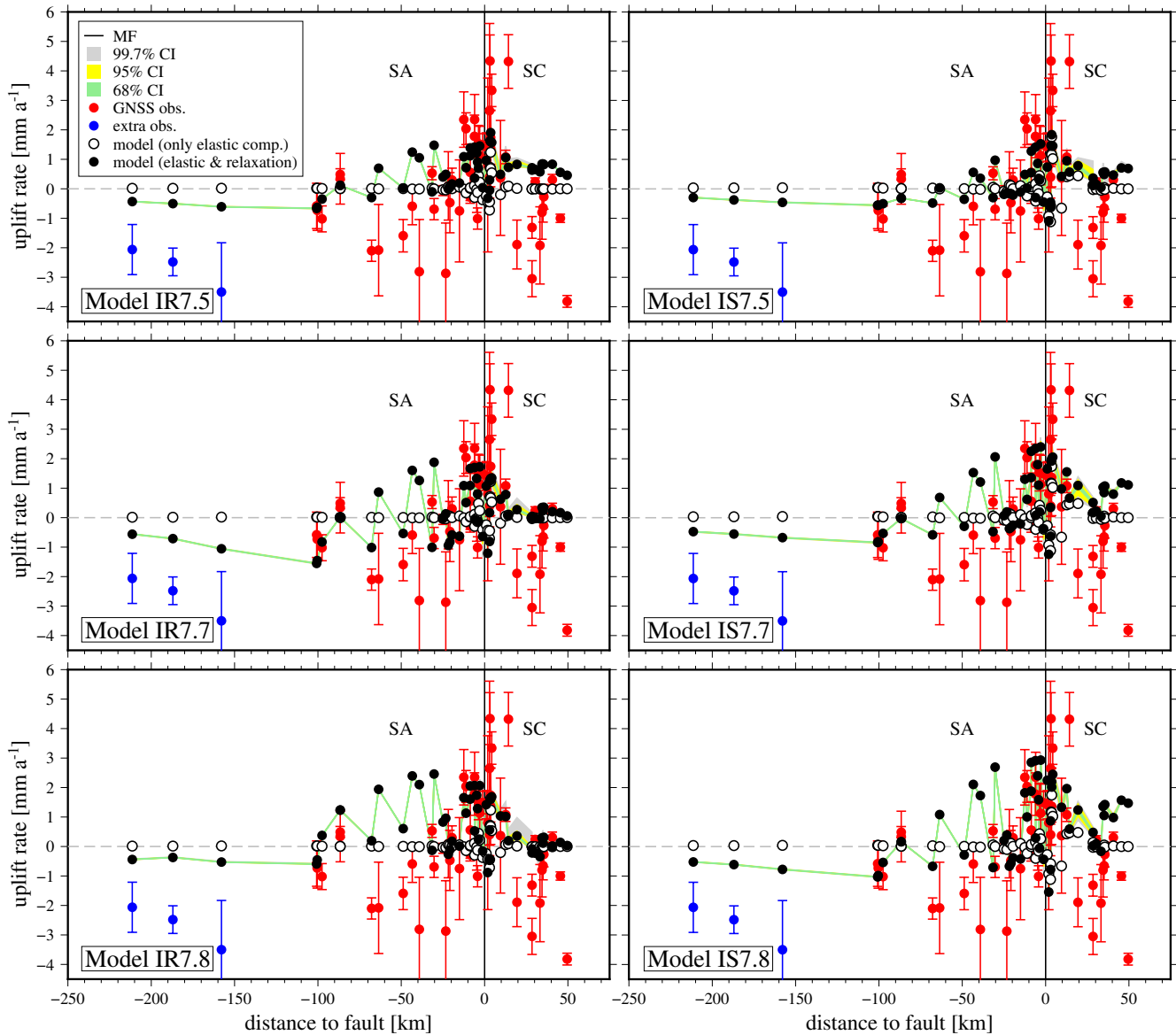


**Figure 7.** Fault-perpendicular profiles of observed and modeled vertical deformation rates across the Magallanes-Fagnano Fault (MF), in Tierra del Fuego, and confidence intervals of the predictions (barely noticeable), taking into account the uncertainties of the calibrated model parameters. Models assuming inclined fault segments are shown here. The narrow deformation belt along the tectonic boundary between the South American and Scotia (SC) plates, about 20–50 km wide, is evident in the uplift pattern close to the MF. This figure is supplemented by Figure S4 in Supporting Information S2, which amplifies the narrow deformation belt along the tectonic boundary.

IR7.7 and IS7.7, Figure 7). However, they all underestimate the observed subsidence, which indicates that this could also be driven by the extensional structures mentioned earlier, and in particular the IB–SSB graben, in addition to the postseismic viscoelastic relaxation (e.g., the site 37 is precisely located in the middle of this graben, see Figure 1). The additional effect of sediment compaction cannot be ruled out either, since these three particular sites are not materialized on bedrock (see Table 1). Overall, the IR7.7 model provides the best fit to these eight observations (Figure 7). Instead, none of the models is able to reproduce the observed subsidence closer to the fault trace and, in fact, several models predict significant uplift in this zone, particularly those models that assume an inclined rupture plane (e.g., models IR7.8 and IS7.8, Figures 6 and 7). This could be an indication of an oversimplification of the models, regarding the strike and length of each of the defined rupture segments, the assumption of a constant coseismic slip along the entire rupture and the disregard of a possible lateral inhomogeneity of the rheological properties of the lithosphere along this section of the transform boundary (i.e., weakening). In any



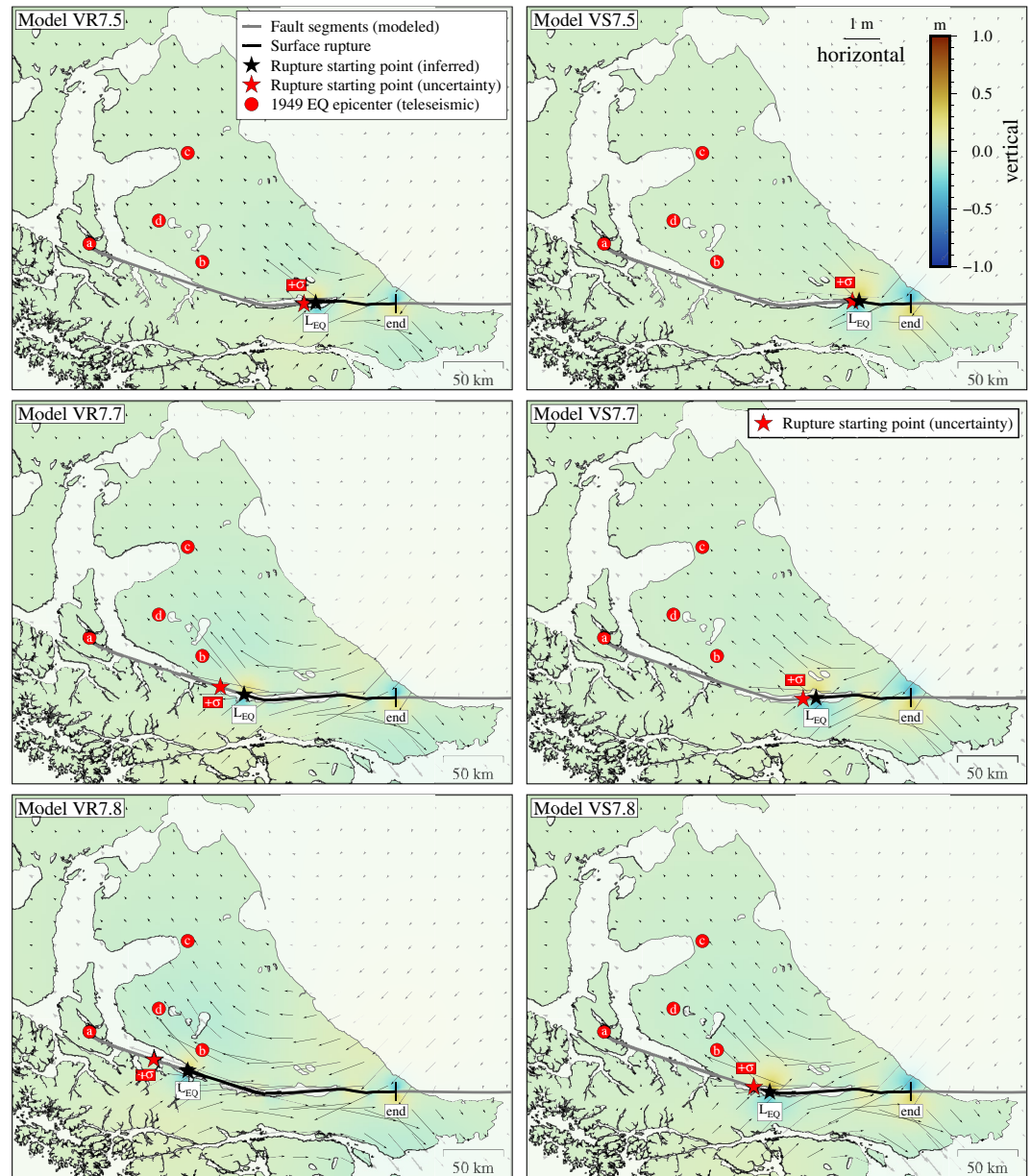


**Figure 8.** Modeling (i.e., simulation) of coseismic deformation associated with the largest of the earthquakes occurred on 17 December 1949, in Tierra del Fuego. Models assuming vertical fault segments are shown here. Also shown is the simulated rupture of length  $L_{EQ}$ , measured westward from the end point, and the corresponding epicenter inferred from teleseismic records according to (a) Zamarbide and Castano (1978), (b) Jaschek et al. (1982), (c) Pelayo and Wiens (1989) and (d) Bondár et al. (2015, updated 2020-07-10).

event, the observational evidence of ongoing deformation so far from the rupture area, still detectable after more than 60 years, points to viscoelastic relaxation at depth, in the mantle. Indeed, Gourmelen and Amelung (2005) studied a very similar situation and concluded that the properties of the elastic lithosphere could be responsible for a long-wavelength deformation, associated to viscous flow in the mantle, that could last several decades after a seismic event, at least 80 years in their case. In practice, they implemented a two-layer rheological model like the one we use, also with a similar effective viscosity between  $10^{18}$  and  $10^{19}$  Pa s, as well as a three-layer model, reaching in both cases the same conclusion.

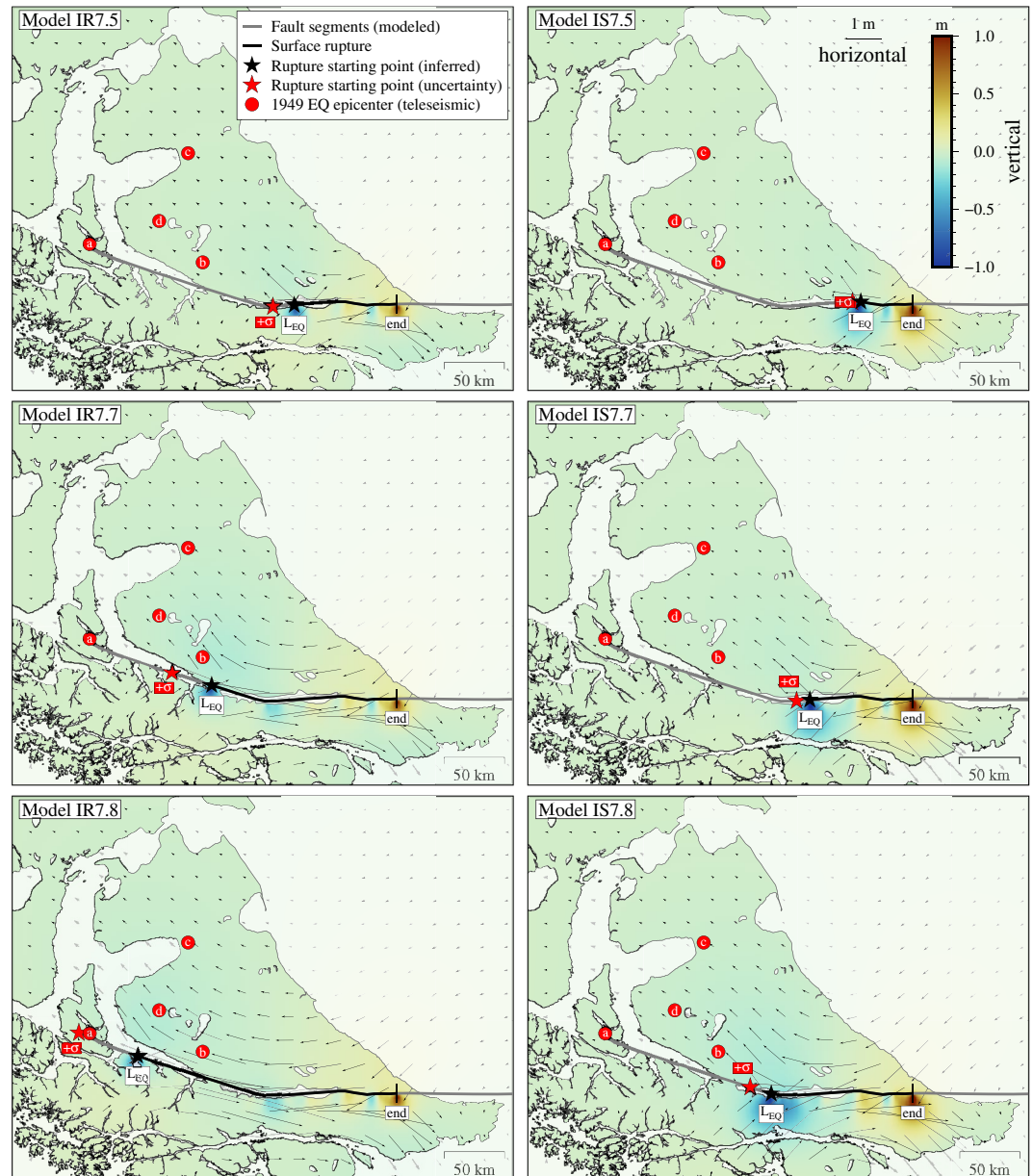


**Figure 9.** Modeling (i.e., simulation) of coseismic deformation associated with the largest of the earthquakes occurred on 17 December 1949, in Tierra del Fuego. Models assuming inclined fault segments are shown here. Also shown is the simulated rupture of length  $L_{EQ}$ , measured westward from the end point, and the corresponding epicenter inferred from teleseismic records according to (a) Zamarbide and Castano (1978), (b) Jaschek et al. (1982), (c) Pelayo and Wiens (1989) and (d) Bondár et al., 2015 (updated 2020-07-10).

### 3.3. Inferred Coseismic and Postseismic Deformation

All models result in coseismic vertical displacements ranging from  $-1$  to  $+1$  m near the fault trace, modulated along it according to the changing orientation of the linear segments with respect to the average direction of slip, with maximum magnitudes at the start and end points of the simulated rupture (Figures 8 and 9). In addition, the inclined models seem to produce more deformation, shifted south toward the SC block. In this regard, eyewitness reports from the 1949 earthquakes indicate vertical offsets of up to 1 m along the eastern shore of LF (sag pond and vertical scarp), a withdrawal of the waters of the lake towards the west and a later wave (seiche) that flooded the same sector near the eastern shore (Costa et al., 2006; Lodolo et al., 2003; Perucca et al., 2015; Yamin &

Anselmi, 2020). Smalley et al. (2003) indicate that most of the reports of surface rupture in the island are indeed associated with the first event and suggest, in agreement with Costa et al. (2006), that the second event may have occurred closer to Punta Arenas (PA in Figure 1). Furthermore, Roy et al. (2019) report evidence of uplifted and subsided blocks during the earthquake, alternating on both sides of the fault main trace, between the eastern shore of LF and Malengüena Hill (i.e., the adopted end point of the coseismic rupture for the modeled earthquake). Our models produce similar features, although the approximate nature of the modeled fault segments, and the simplifications made on the magnitude of the coseismic slip (i.e., here assumed to be uniform along the rupture length), make any specific correspondence difficult.

Both the long-term slip rate adopted for each model, either from Roy et al. (2019) or Sandoval and De Pascuale (2020), and of course the moment magnitude assumed, appear to be critical in modeling the coseismic deformation during the 1949 earthquake and the subsequent viscoelastic relaxation in the island, up to the present. Indeed, and in addition to the previously mentioned differences in the inferred locking depths (i.e., in the width of the dislocation planes), the large differences in the estimated length of the rupture  $L_{EQ}$  between models VR7.5, VR7.7, VR7.8, IR7.5, IR7.7, and IR7.8 and models VS7.5, VS7.7, VS7.8, IS7.5, IS7.7, and IS7.8, respectively, play a key role. For example, only models VR7.7, VR7.8, IR7.7, and IR7.8 result in a rupture that runs along the fault bend located in the western part of Lake Fagnano. That is, none of the models employing the lowest moment magnitude (i.e., 7.5) does so. It is worth noting that there are no precise estimates of the length of the coseismic rupture associated with either of the two earthquakes that occurred in December 1949. For example, Costa et al. (2006) suggested a rupture length between 250 and 1,000 km, most provably near the lower end, based on earthquake scaling relationships (i.e., regressions) by Liu-Zeng et al. (2005) and assuming at that time a coseismic slip of 4–5 m. Abascal and González Bonorino (2014) estimated a minimum length of 130 km for the rupture, or at least for a section of it, based on the location of the aftershocks that followed both events. With a similar reasoning González Bonorino et al. (2011) suggested a total rupture length of ~300 km. Stirling et al. (2013) give an up-to-date set of earthquake scaling relationships, intended for seismic hazard analysis, indicating their applicability to different tectonics regimes. Given the slip rate  $\dot{s} < 10 \text{ mm a}^{-1}$  along the MF in Tierra del Fuego we could apply here the relationship found by Wesnousky (2008) which relates the surface rupture length  $L_{EQ}$  with the moment magnitude  $M_w$ , resulting in a length of ~290 km for an earthquake of  $M_w = 7.7$  along a predominantly strike-slip fault. Whereas, assuming this moment magnitude all our inferred rupture lengths fall below the latter estimate, models VR7.7 and IR7.7 are consistent with ruptures up to 170 and 230 km, respectively, with 95% confidence (i.e., at a two-sigma level). Also, only models VR7.7, VR7.8, IR7.7, IR7.8, and IS7.8 seem to be able to locate the rupture starting point close to the seismologically estimated epicenters (Figures 8 and 9). Of course, this scenario would imply a primarily unilateral (i.e., the epicenter near one end), west-to-east rupture, controlled by fault irregularities (Sibson, 1989), the most prominent of which are the jog linking two en échelon segments of MF on Dawson Island (DI, in the mouth of Almirantazgo Sound, Figure 1) and the fault bend in Lake Fagnano. For example, a similar unilateral propagation was found by Lin et al. (2003) studying the 2001  $M_w$  7.8 Central Kunlun earthquake, in China, along a left-lateral strike-slip fault. They found that, although the rupture started bilaterally, it eventually extended 370 km eastward and only 30 km westward from the estimated epicenter. Nevertheless, had we adopted a more realistic (i.e., non-uniform) coseismic slip distribution, rather than adopting a common value along all fault segments, the inferred rupture lengths would have been longer in all cases, which in turn would have resulted in better agreement between our models, the scaling regressions and the multiple epicenter relocations (assuming a maximum slip of ~6 m, for example, and gradually reaching a null slip at both ends). However, the fact that the rupture was probably mostly subaqueous makes a more precise modeling difficult due to the lack of direct observations.

Significant deformation rates covering the entire Tierra del Fuego island are obtained letting the simulations evolve to the present (i.e., to the mean observational epoch of the GNSS data), with horizontal and vertical rates of up to ~0.8 and  $\pm 2.5 \text{ mm a}^{-1}$ , respectively. All models produce a similar checkered (i.e., gridded) vertical relaxation pattern, roughly symmetrical with respect to the simulated ruptures, with subsidence and uplift zones located to the northwest and northeast of them, respectively, and an opposite pattern to the south (Figures 10 and 11). The magnitude and orientation of the predicted horizontal deformation rates follow exactly the same pattern. However, models with non-vertical rupture planes shift the line of symmetry southward, parallel to the modeled ruptures, toward the hanging wall (a shift of ~50 km in the case of model IR7.7, for example). Moreover, all models place the center of relaxation uplift offshore, in the Atlantic Ocean, and conversely, the center of subsidence in the northern part of the island, for example, directly inside Inútil Bay in the case of models IR7.7 and



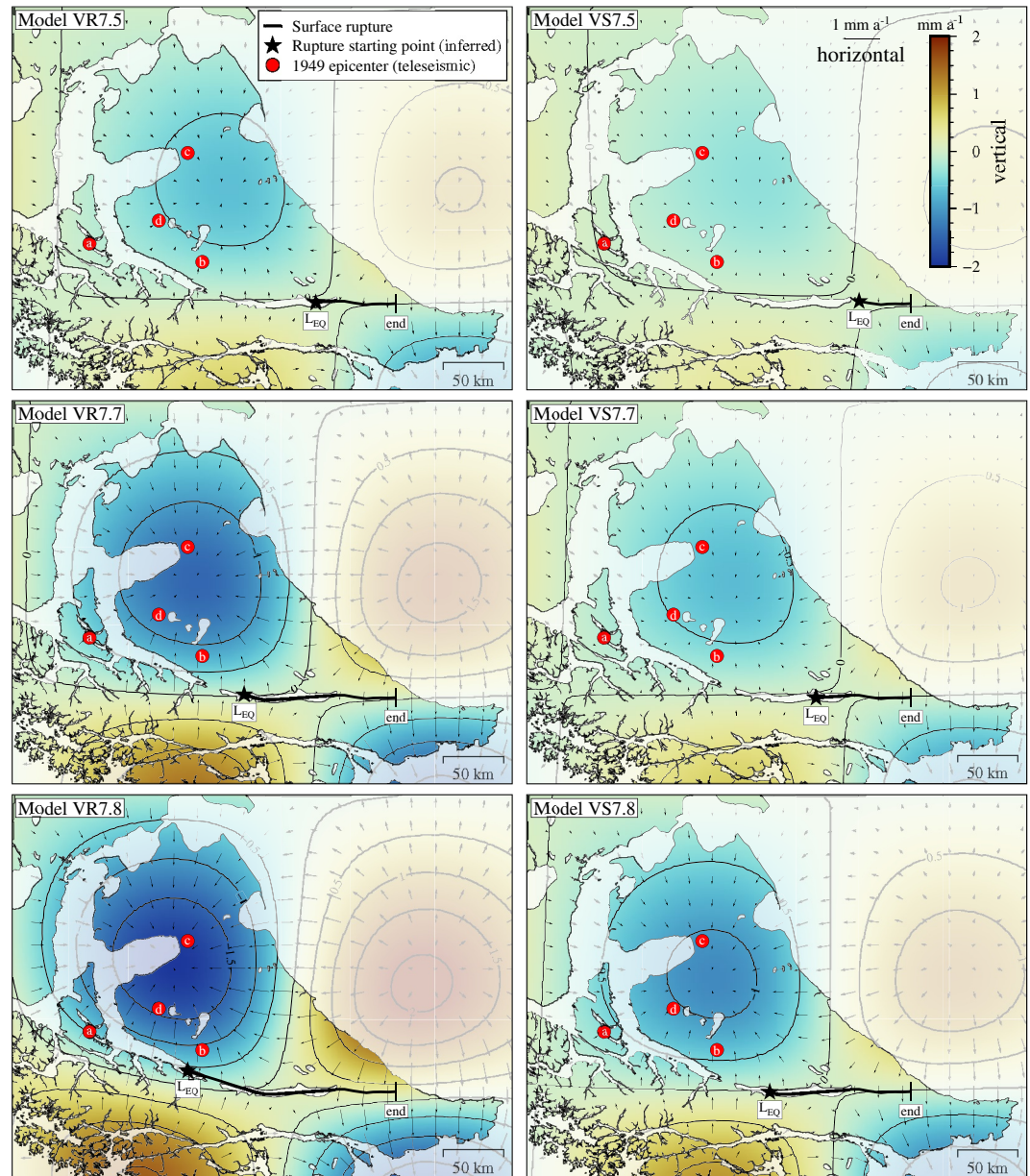


**Figure 10.** Modeling (i.e., simulation) of deformation rates, at the mean epoch of the Global Navigation Satellite System observations, due to postseismic viscoelastic relaxation approximately 60 years after the largest of the earthquakes occurred on 17 December 1949, in Tierra del Fuego. Models assuming vertical fault segments are shown here. Also shown is the simulated rupture of length  $L_{EQ}$ , measured westward from the end point, and the corresponding epicenter inferred from teleseismic records according to (a) Zamarbide and Castano (1978), (b) Jaschek et al. (1982), (c) Pelayo and Wiens (1989) and (d) Bondár et al. (2015), (updated 2020-07-10).

IR7.8, almost a hundred kilometers north from the MF trace. Although we will not discuss it here, at this point a question arises: what could be the cumulative effect on the pre-existing extensional structures to the north of the island (e.g., Diraison et al., 1997; Menichetti et al., 2008) of this pattern of subsidence possibly driven by flow in the mantle and repeated every seismic cycle (for example, every  $\sim 1000$  years, see below)?

As mentioned earlier, it was not necessary to include any logarithmic or exponential terms in any of the trajectory models during the analysis of the GNSS position time series. However, this does not imply that there is actually no postseismic relaxation process ongoing in the study area. In fact, the comparison between our observations and the models clearly suggests the opposite. However, in this case all models indicate that during the time

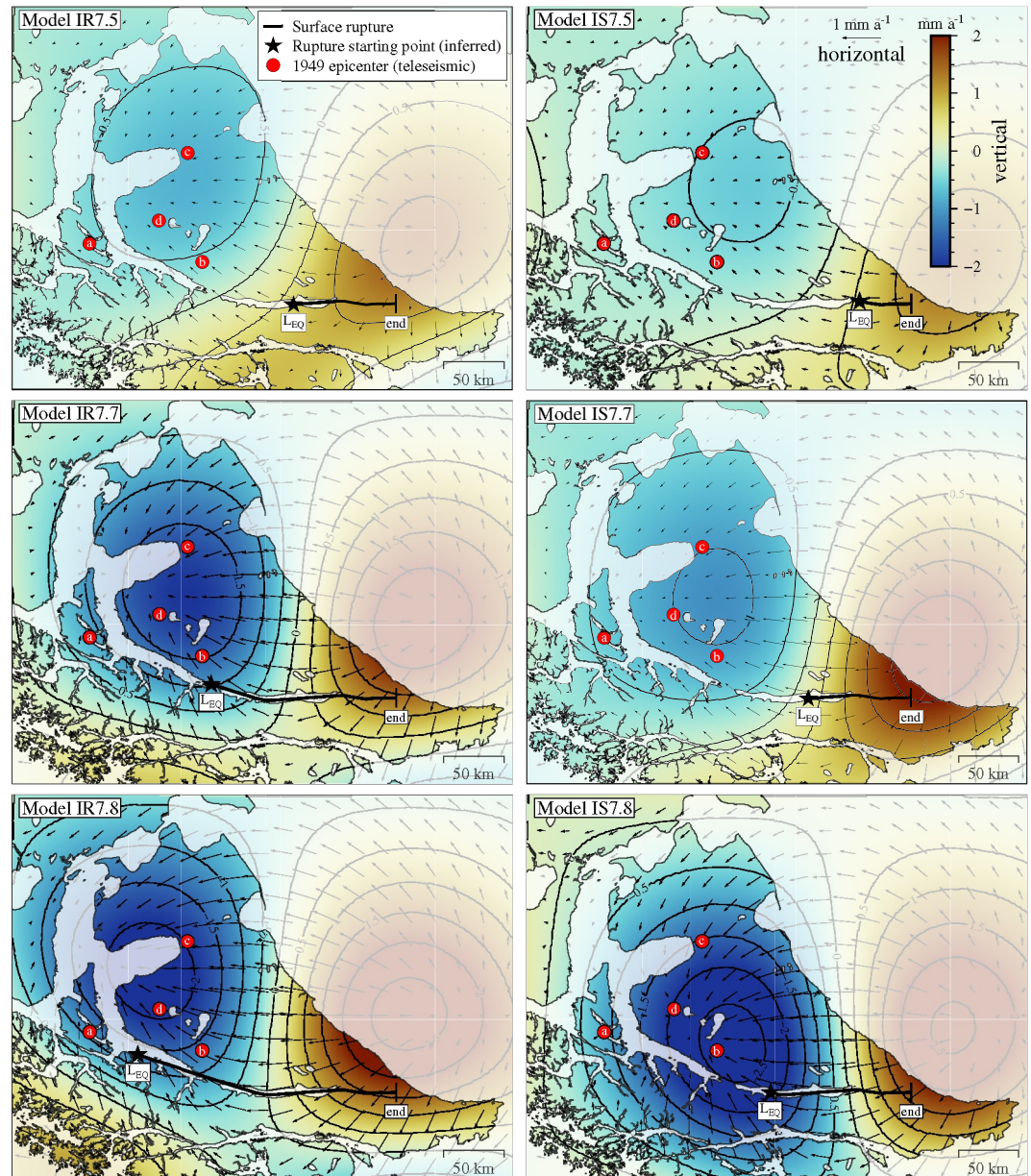


**Figure 11.** Modeling (i.e., simulation) of deformation rates, at the mean epoch of the Global Navigation Satellite System observations, due to postseismic viscoelastic relaxation approximately 60 years after the largest of the earthquakes occurred on 17 December 1949, in Tierra del Fuego. Models assuming inclined fault segments are shown here. Also shown is the simulated rupture of length  $L_{EQ}$ , measured westward from the end point, and the corresponding epicenter inferred from teleseismic records according to (a) Zamarbide and Castano (1978), (b) Jaschek et al. (1982), (c) Pelayo and Wiens (1989) and (d) Bondár et al. (2015), (updated 2020-07-10).

span of the GNSS measurements all relaxation trajectories should present a nearly constant slope (i.e., constant deformation rate) in all components (e.g., Figure 12). In essence, this is why the secular velocity and any possible time-dependent relaxation affecting a site cannot be decoupled here using only the GNSS data, so late after the earthquake. Indeed, the assumed effective viscosity for the underlying half-space in all models implies that the GNSS measurements were collected between 8.5 and 13 Maxwell relaxation times  $t_R$  after this particular event. Even in the case of the vertical deformation, which is more pronounced than the horizontal, the increased observational noise (i.e., the uncertainties in the vertical GNSS solutions) makes it impossible to separate the two processes with any acceptable confidence during the analysis of the isolated time series. Similarly, this GNSS



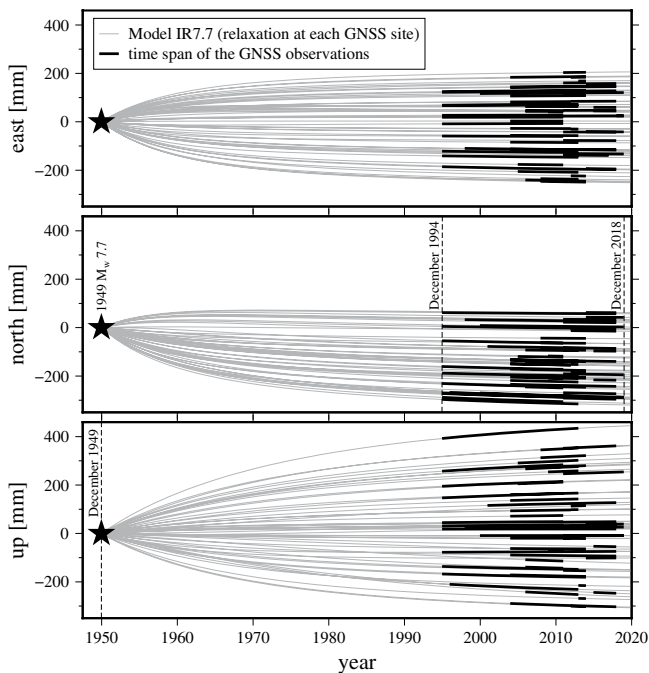


**Figure 12.** Example of modeled (i.e., simulated) trajectories, for all the analyzed Global Navigation Satellite System sites, due to postseismic viscoelastic relaxation after the largest of the earthquakes occurred on 17 December 1949, in Tierra del Fuego. During the observation time frame all trajectories exhibit an almost constant slope, making it difficult to decouple the relaxation from the secular motion.

uncertainties reported by the different authors for the coseismic offset  $s_{EQ}$  and the slip rate  $\dot{s}$  (see Table 3). Of course, the seismic moment  $M'_0$  possibly accumulated since 1949 can be expressed also as an equivalent moment magnitude

$$M'_w = \frac{2}{3} (\log M'_0 - 9.1) \quad (8)$$

resulting at present (i.e., the year 2021) in a feasible moment magnitude  $M_w \simeq 7$  for a damaging earthquake in Tierra del Fuego (Table 3). Note that these estimated magnitudes shall be considered as approximate. On one hand, in this simple cumulative moment budget computation we have not considered the seismic moment released by those low magnitude earthquakes that occurred during that period. On the other hand, we consider here that all the previously accumulated seismic moment was completely released during the 1949 earthquakes and this may not be the case.

The already discussed differences in the locking depth translate here into seismic moment deficit rates which are, when employing Sandoval and De Pascales's slip rate, twice as high as those resulting from models employing Roy et al.'s estimate. In other words, given a length of locked fault section, models employing Roy et al.'s estimate (e.g., VR7.7 and IR7.7) would require twice the time for the accumulated moment to reach a certain threshold, compared to the time needed for models employing Sandoval and De Pascales's estimate (e.g., VS7.7 and IS7.7) or, conversely, for a given rupture length, models employing Roy et al.'s estimate would imply a 50% lower moment release after the same interseismic period. This significant disparity can be attributed solely to the difference in the long-term slip rate estimates made by Roy et al. (2019) and Sandoval and De Pascale (2020), as all other model characteristics and observational constraints are common. On the other hand, both recurrence intervals  $T$ , independent but consistent with each of our 12 models, appear to be in agreement with previous determinations. For example, following similar reasoning several intervals have already been proposed:  $1,000 \pm 215$  years (Roy et al., 2019, in fact, for half of our models our estimate is the same), between 800 and

data set cannot effectively constrain the parameters of the rheological model employed here, namely the thickness  $H$  of the elastic layer and the viscosity  $\eta$  of the underlying half-space.

### 3.4. Seismic Aftermath

Using the corresponding a priori slip rate  $\dot{s}$  associated to each model it is possible to estimate the current seismic moment accumulation rate (i.e., the moment deficit rate), per unit of length, as

$$\frac{\dot{M}_0}{L} = \mu \dot{s} W \quad (5)$$

in addition, and directly from the given slip rate  $\dot{s}$ , coseismic offset  $s_{EQ}$  and moment magnitude  $M_w$  employed in this study, it is also possible to approximate a recurrence interval for damaging earthquakes in the island as

$$T = \frac{s_{EQ}}{\dot{s}} \quad (6)$$

as well as the seismic moment accumulated in the interval  $\Delta T = 2021 - 1949$  since the last event as

$$M'_0 = \frac{\dot{s} M_0 \Delta T}{s_{EQ}} \quad (7)$$

While these last two values are in fact independent of our calibrated model parameters, they are also consistent with them. Estimates of all these quantities related to the seismic cycle in the island can be obtained for each of the calibrated models, including their corresponding uncertainties through a Monte Carlo error propagation scheme, taking into account here not only the variances of the estimates of the parameters of our models, but also the

**Table 3**  
*Seismic Parameters Consistent With the Respective Calibrated Models*

Model	W [km]	$\dot{M}_0/L$ [ $10^{12}$ N m a <sup>-1</sup> km <sup>-1</sup> ]	$T^a$ [a]	$M_0^a$ [ $10^{19}$ N m]	$M_w^a$
VR7.5	18.1 ± 2.5	3.47 ± 0.69	957 ± 165	1.73 ± 0.28	6.75 ± 0.05
IR7.5	14.8 ± 2.7	2.84 ± 0.67	idem	idem	idem
VR7.7	20.4 ± 3.0	3.92 ± 0.80	idem	3.45 ± 0.57	6.95 ± 0.05
IR7.7	16.6 ± 3.1	3.19 ± 0.75	idem	idem	idem
VR7.8	20.4 ± 2.9	3.92 ± 0.79	idem	4.88 ± 0.80	7.05 ± 0.05
IR7.8	16.4 ± 3.1	3.14 ± 0.75	idem	idem	idem
VS7.5	28.4 ± 3.0	6.65 ± 1.32	793 ± 161	2.11 ± 0.40	6.81 ± 0.06
IS7.5	27.8 ± 3.9	6.51 ± 1.42	idem	idem	idem
VS7.7	29.7 ± 2.9	6.95 ± 1.35	idem	4.21 ± 0.79	7.01 ± 0.06
IS7.7	29.7 ± 3.9	6.94 ± 1.48	idem	idem	idem
VS7.8	30.6 ± 2.7	7.16 ± 1.35	idem	5.95 ± 1.12	7.11 ± 0.06
IS7.8	30.2 ± 3.9	7.07 ± 1.50	idem	idem	idem

*Note.* W: downdip width of faulting planes;  $\dot{M}_0/L$ : seismic moment accumulation rate, per unit of length; T: recurrence interval for damaging earthquakes;  $M_0^a$ : seismic moment accumulated, along the modeled rupture length  $L_{EQ}$ , between 1949 and 2021;  $M_w^a$ : equivalent moment magnitude at 2021.

<sup>a</sup>These columns are independent of, but consistent with, the calibrated parameters of each model.

1000 years (González Bonorino et al., 2011), ~750 years (Smalley et al., 2003). Also, using an entirely different approach, Waldmann, Anselmetti, et al. (2010) proposed a bimodal recurrence with two periods of ~350 and ~850 years, respectively, based on a dated sequence of mass-wasting deposits in LF (i.e., from ~11,000 years ago to present) produced by seismic shaking. Nonetheless, none of the inferred recurrence intervals seem to agree with the short span of only 70 years between the occurrence of the major events of 1879 and 1949. Waldmann, Anselmetti, et al. (2010) pointed this out and suggested, based on paleoseismic studies of the San Andreas fault system (Grant & Sieh, 1994; Jacoby et al., 1988), the existence of *supercycles* (i.e., temporal clusters of event occurrences). These cycles could end in two events, along different sections of the MF or along the same section but with partial stress release. The evidence found by Pedrera et al. (2014) studying disturbed trees along the MF trace points to the latter.

#### 4. Conclusions

We generated numerical models for the current seismic cycle in Tierra del Fuego since the major 1949 earthquake, consistently analyzing geodetic, geological and seismological observations. The models VR7.7 and IR7.7, constrained by the geological estimate made by Roy et al. (2019) for the slip rate accommodated across the Magallanes-Fagnano Fault, seem to be the most consistent with the geodetic and seismological data in the island, especially the one considering inclined fault planes. In particular, the predictions of these models are in good agreement with the numerous epicenter relocations of the 1949 events, the proposed rupture lengths, the observed shallow, intracrustal seismicity, and both horizontal and vertical deformation rates measured by GNSS. The consistency with the GNSS observations is only possible if an ongoing postseismic viscoelastic relaxation process is taken into account. In addition, the coseismic deformation predicted by those two models appears to agree with witness reports and geologic evidence along the area that ruptured in 1949. The model considering inclined fault planes is also in excellent agreement with recently obtained moment tensor solutions for a  $M_b = 4.2$  event which occurred in the island in 2009 (Bollini, 2021). In contrast, models adopting the Magallanes-Fagnano Fault slip rate estimate derived by Sandoval and De Pascale (2020) produce larger discrepancies with the geodetic evidence available to date, and can only be made consistent with the GNSS data set by excessively large locking depths along the faulting plane.

In summary, the estimated parameters of the preferred model indicate a seismogenic layer thickness of  $15 \pm 3$  km in Tierra del Fuego, fault planes inclined  $63^\circ \pm 4^\circ$ , dipping to the south, and a rupture length, for the largest of the

1949 earthquakes, of about  $160 \pm 40$  km. Along the sections of the Magallanes-Fagnano Fault in the island these results are also consistent with a moment deficit rate, per unit of length, of approximately  $3.2 \pm 0.8 \times 10^{12}$  N m  $a^{-1}$  km $^{-1}$ , and a cumulative seismic moment, to date, equivalent to an earthquake of magnitude  $M_w \simeq 7$ . Clearly, by not taking into account the ongoing postseismic relaxation process in our previous work (L. Mendoza et al., 2015), we may have underestimated the width of those fault planes that could dislocate in a complete coseismic rupture, that is, the next major event, by as much as 50%. The results also indicate the prevalence of the postseismic viscoelastic relaxation process, more than 60 years after the largest registered seismic event in Tierra del Fuego, and probably related to viscous flow in the mantle. This ongoing process may be responsible, at present, for deformation rates of up to 0.8 and  $\pm 2.5$  mm  $a^{-1}$ , in the horizontal and vertical directions, respectively. Postseismic relaxation appears to be affecting the entire region up to  $\sim 200$  km away from the Magallanes-Fagnano Fault in Tierra del Fuego, with a main area of subsidence located approximately at Inútil Bay, on the shores of the Strait of Magellan. The presented results confirm the need for an update of the seismic risk assessment in Tierra del Fuego (Abascal & Gonzáles Bonorino, 2014).

The application of the PPP method to analyze a GNSS data set in Tierra del Fuego covering a long period of time yields results as precise and consistent as the differential approach. A significant advantage of this method is that the vertical coordinates and estimated rates are absolute and refer to a common, stable and global origin. In fact, although the observed vertical rates were not used here to constrain the model parameters, these observations are most sensitive to the ongoing viscoelastic relaxation process. In this regard, the inferred uplift and subsidence pattern indicates the need to extend the geographic coverage of the geodetic observations to the west of the island, to Chilean territory, and also to the continental part of southern Patagonia. Of course, more data will also help to confirm or rule out the possible contribution of other processes to the observed deformations. For example, the GNSS velocities seem to agree with geological evidence of rapid tectonic uplift along the trace of the Magallanes-Fagnano Fault. The observations also suggest the possible existence of ongoing subsidence related to some extensional structures in the northern part of the island, and in particular the Inútil Bay and San Sebastián Bay graben. The same observations indicate that some lateral movement could also be accommodated across these structures. Similarly, the GNSS velocities seem to agree with the geologic evidence of current slip across the Deseado Fault, north of the Magallanes-Fagnano Fault (De Pascale, 2021; Klepeis, 1994). Additional observations and more complex multi-fault modeling will be needed in the future to confirm this.

#### Acknowledgments

This research is part of a bilateral scientific cooperation project between Universidad Nacional de La Plata (Argentina), Facultad de Ciencias Astronómicas y Geofísicas, and Technische Universität Dresden (Germany), Institut für Planetare Geodäsie, funded by the Agencia Nacional de Promoción de la Investigación, el Desarrollo Tecnológico y la Innovación (Argentina), through the Fondo para la Investigación Científica y Tecnológica (grant PICT-2015-1776). Part of the earlier fieldwork was funded by the German Research Foundation (grant DI 473/44-1), Ministerio de Ciencia, Tecnología e Innovación (Argentina) and the Internationales Büro des Bundesministerium für Bildung und Forschung (Germany, Project No. AL/PA01-UV II/01). The authors special thanks to the Echeverría family of Bahía El Torito and to the de Larminat family of Ea. Despedida for their support and hospitality during the many field works. The authors thank the Prefectura Naval Argentina, Destacamento Lago Fagnano, for their operational support during field work at the lake. The authors also thank the Goodall family of Ea. Harberton for their support during field work at Beagle Channel. Some field work was carried out within Tierra del Fuego National Park and the authors sincerely thank all the staff for support, advice and permission of our activities. E. R. Marderwald was funded by post-graduate scholarships from the Consejo Nacional de Investigaciones Científicas y Técnicas (Argentina). The authors thank Editor in Chief Taylor Schildgen and Associate Editor Marcelo Farias for thoughtful comments. This manuscript improved substantially from reviews by Gregory De Pascale and Joseph Martinod.

#### Data Availability Statement

Open-access datasets of all the employed position time series, for all the GNSS sites and since 1994, can be retrieved from PANGAEA (L. Mendoza et al., 2021). Open-access datasets of all continuously operating GNSS station employed in this research were provided by IGS at <https://cddis.nasa.gov/archive/gps/data/daily/> (see Johnston et al., 2017), by IGN at <https://www.ign.gov.ar/NuestrasActividades/Geodesia/Ramsac/DescargaRinex> (see Piñón et al., 2018) and by CSN at <http://gps.csn.uchile.cl/data/> (see Barrientos et al., 2018). Alternatively, the IGN data set can be retrieved from MAGGIA's open-access mirror at <https://wikilen.fcaglp.unlp.edu.ar/gnss/>.

#### References

- Abascal, L. d. V., & Gonzáles Bonorino, G. (2014). Evaluación del riesgo sísmico para Tolhuin, Tierra del Fuego, Argentina, aplicando el programa Selena. *Revista de Geología Aplicada a la Ingeniería y al Ambiente*, 33, 93–106. Retrieved from <https://www.editoresasagai.org.ar/ojs/index.php/rgaia/article/view/75>
- Afonso, J. C., Salajegheh, F., Szwilius, W., Ebbing, J., & Gaina, C. (2019). A global reference model of the lithosphere and upper mantle from joint inversion and analysis of multiple data sets. *Geophysical Journal International*, 217(3), 1602–1628. <https://doi.org/10.1093/gji/ggz094>
- Ammirati, J.-B., Flores, M. C., & Ruiz, S. (2020). Seismicity along the Magallanes-Fagnano fault system. *Journal of South American Earth Sciences*, 103, 102799. <https://doi.org/10.1016/j.jsames.2020.102799>
- Bagnardi, M., & Hooper, A. (2018). Inversion of surface deformation data for rapid estimates of source parameters and uncertainties: A Bayesian approach. *Geochemistry, Geophysics, Geosystems*, 19(7), 2194–2211. <https://doi.org/10.1029/2018gc007585>
- Barbot, S. (2014). *Relax v1.0.7 (software)*. Retrieved from [https://geodynamics.org/cig/software/relax/\(RELAX\)](https://geodynamics.org/cig/software/relax/(RELAX))
- Barbot, S., & Fialko, Y. (2010a). Fourier-domain Green's function for an elastic semi-infinite solid under gravity, with applications to earthquake and volcano deformation. *Geophysical Journal International*, 182(2), 568–582. <https://doi.org/10.1111/j.1365-246x.2010.04655.x>
- Barbot, S., & Fialko, Y. (2010b). A unified continuum representation of post-seismic relaxation mechanisms: Semi-analytic models of afterslip, poroelastic rebound and viscoelastic flow. *Geophysical Journal International*, 182(3), 1124–1140. <https://doi.org/10.1111/j.1365-246x.2010.04678.x>
- Barrientos, S., & National Seismological Center (CSN) Team. (2018). The seismic network of Chile. *Seismological Research Letters*, 89(2A), 467–474. <https://doi.org/10.1785/0220160195>

- Bevis, M., & Brown, A. (2014). Trajectory models and reference frames for crustal motion geodesy. *Journal of Geodynamics*, 88(3), 283–311. <https://doi.org/10.1007/s00190-013-0685-5>
- Bird, P. (2003). An updated digital model of plate boundaries. *Geochemistry, Geophysics, Geosystems*, 4(3), 1027. <https://doi.org/10.1029/2001GC000252>
- Boehm, J., Werl, B., & Schuh, H. (2006). Troposphere mapping functions for GPS and very long baseline interferometry from European Centre for Medium-Range Weather Forecasts operational analysis data. *Journal of Geophysical Research*, 111(B2), B02406. <https://doi.org/10.1029/2005JB003629>
- Bollini, M. C. (2021). *Modelado de fuente sísmica mediante inversión de forma de onda. Aplicación en Tierra del Fuego (Doctoral dissertation)*, Facultad de Ciencias Astronómicas y Geofísicas. Universidad Nacional de La Plata. Retrieved from <http://sedici.unlp.edu.ar/handle/10915/124830>
- Bondár, I., Engdahl, E. R., Villaseñor, A., Harris, J., & Storchak, D. (2015). ISC-GEM: Global instrumental earthquake catalogue (1900–2009), II. location and seismicity patterns. *Physics of the Earth and Planetary Interiors*, 239, 2–13. <https://doi.org/10.1016/j.pepi.2014.06.002>
- Bos, M. S., Fernandes, R. M. S., Williams, S. D. P., & Bastos, L. (2012). Fast error analysis of continuous GNSS observations with missing data. *Journal of Geodynamics*, 87(4), 351–360. <https://doi.org/10.1007/s00190-012-0605-0>
- Bruhat, L. (2019). A physics-based approach of deep interseismic creep for viscoelastic strike-slip earthquake cycle models. *Geophysical Journal International*, 220(1), 79–95. <https://doi.org/10.1093/gji/ggz426>
- Buffoni, C., Sabbione, N. C., Connon, G., & Hormaechea, J. L. (2009). Localización de hipocentros y determinación de su magnitud en Tierra del Fuego y zonas aledañas. *Geoacta*, 34(2), 75–85. Retrieved from [http://www.scielo.org.ar/scielo.php?script=sci\\_arttext&pid=S1852-77442009000200003](http://www.scielo.org.ar/scielo.php?script=sci_arttext&pid=S1852-77442009000200003)
- Buffoni, C., Schimmel, M., Sabbione, N. C., Rosa, M. L., & Connon, G. (2017). Rayleigh waves from correlation of seismic noise in Great Island of Tierra del Fuego, Argentina: Constraints on upper crustal structure. *Geodesy and Geodynamics*, 9(1), 2–12. <https://doi.org/10.1016/j.geog.2017.11.006>
- Buffoni, C., Schimmel, M., Sabbione, N. C., Rosa, M. L., & Connon, G. (2019). Crustal structure beneath Tierra del Fuego, Argentina, inferred from seismic P-wave receiver functions and ambient noise autocorrelations. *Tectonophysics*, 751, 41–53. <https://doi.org/10.1016/j.tecto.2018.12.013>
- Bürgmann, R., & Dresen, G. (2008). Rheology of the lower crust and upper mantle: Evidence from rock mechanics, geodesy, and field observations. *Annual Review of Earth and Planetary Sciences*, 36(1), 531–567. <https://doi.org/10.1146/annurev.earth.36.031207.124326>
- Capaccioni, B., Menichetti, M., Renzulli, A., Tassone, A., & Huertas, A. D. (2013). Thermal waters of “tectonic origin”: The alkaline, Na-HCO<sub>3</sub> waters of the Rio Valdez geothermal area (Isla Grande de Tierra del Fuego, Argentina). *Geofluids*, 13(1), 21–31. <https://doi.org/10.1111/gfl.12005>
- Chen, G., & Herring, T. A. (1997). Effects of atmospheric azimuthal asymmetry on the analysis of space geodetic data. *Journal of Geophysical Research: Solid Earth*, 102(B9), 20489–20502. <https://doi.org/10.1029/97jb01739>
- Connon, G. C., Bollini, M. C., Sabbione, N. C., & Hormaechea, J. L. (2021). *Complemento 2017–2020 del Catálogo Sismológico de Referencia de Tierra del Fuego (techreport) (FCAG, UNLP)*. Retrieved from <http://sedici.unlp.edu.ar/handle/10915/119549>
- Costa, C. H., Smalley, R., Schwartz, D. P., Stenner, H. D., Ellis, M., Ahumada, E. A., & Velasco, M. S. (2006). Paleoseismic observations of an onshore transform boundary: The Magallanes-Fagnano Fault, Tierra del Fuego, Argentina. *Revista de la Asociación Geológica Argentina*, 61(4), 647–657. Retrieved from <http://www.scielo.org.ar/pdf/raga/v61n4/v61n4a17.pdf>
- Dach, R., Lutz, S., Walser, P., & Fridez, P. (Eds.). (2015). *Bernese GNSS software version 5.2*. Bern Open Publishing. Retrieved from <https://boris.unibe.ch/72297/>
- De Pascale, G. P. (2021). Comment on “Crustal faults in the Chilean Andes: Geological constraints and seismic potential” by Santibáñez et al. (2019). *Andean Geology*, 46(1), 32–65. <https://doi.org/10.5027/andgeoV48n1-3310>
- DeMets, C., Gordon, R. G., & Argus, D. F. (2010). Geologically current plate motions. *Geophysical Journal International*, 181(1), 1–80. <https://doi.org/10.1111/j.1365-246x.2009.04491.x>
- Di Giacomo, D., Bondár, I., Storchak, D. A., Engdahl, E. R., Bormann, P., & Harris, J. (2015). ISC-GEM: Global instrumental earthquake catalogue (1900–2009), III. Re-computed MS and mb, proxy MW, final magnitude composition and completeness assessment. *Physics of the Earth and Planetary Interiors*, 239, 33–47. <https://doi.org/10.1016/j.pepi.2014.06.005>
- Di Giacomo, D., Engdahl, E. R., & Storchak, D. A. (2018). The ISC-GEM earthquake catalogue (1904–2014): Status after the extension project. *Earth System Science Data*, 10(4), 1877–1899. <https://doi.org/10.5194/essd-10-1877-2018>
- Dietrich, R., Dach, R., Engelhardt, G., Ihde, J., Korth, W., Kutterer, H.-J., et al. (2001). ITRF coordinates and plate velocities from repeated GPS campaigns in Antarctica - An analysis based on different individual solutions. *Journal of Geodynamics*, 74(11–12), 756–766. <https://doi.org/10.1007/s001900000147>
- Diraison, M., Cobbold, P. R., Gapais, D., & Rossello, E. A. (1997). Magellan strait: Part of a Neogene rift system. *Geology*, 25(8), 7032. [https://doi.org/10.1130/0091-7613\(1997\)025<0703:mspan>2.3.co;2](https://doi.org/10.1130/0091-7613(1997)025<0703:mspan>2.3.co;2)
- Dolan, J. F., & Meade, B. J. (2017). A comparison of geodetic and geologic rates prior to large strike-slip earthquakes: A diversity of earthquake-cycle behaviors? *Geochemistry, Geophysics, Geosystems*, 18(12), 4426–4436. <https://doi.org/10.1002/2017gc007014>
- Drewes, H. (2009). The actual plate kinematic and crustal deformation model APKIM2005 as basis for a non-rotating ITRF. In H. Drewes (Ed.), *Geodetic reference frames* (Vol. 134, pp. 95–99). Springer Berlin Heidelberg. [https://doi.org/10.1007/978-3-642-00860-3\\_15](https://doi.org/10.1007/978-3-642-00860-3_15)
- Esteban, F. D., Tassone, A., Lodolo, E., Menichetti, M., Lippai, H., Waldmann, N., et al. (2014). Basement geometry and sediment thickness of lago Fagnano (Tierra del Fuego). *Andean Geology*, 41(2), 293–313. <https://doi.org/10.5027/andgeoV41n2-a02>
- Fattaruso, L. A., Cooke, M. L., & Dorsey, R. J. (2014). Sensitivity of uplift patterns to dip of the San Andreas fault in the Coachella Valley, California. *Geosphere*, 10(6), 1235–1246. <https://doi.org/10.1130/ges01050.1>
- Febrer, J. M., Plasencia, M. P., & Sabbione, N. C. (2000). Local and regional seismicity from Ushuaia broadband station observations (Tierra del Fuego). *Terra Antarctica*, 2(8), 35–40. Retrieved from <https://www.semanticscholar.org/paper/Local-and-Regional-Seismicity-from-Ushuaia-Station-Febrer-Plasencia/7e27c2a162e5e87d616b019ee58808390c8dd524>
- Fritsche, M., Dietrich, R., Knöfel, C., Rülke, A., Vey, S., Rothacher, M., & Steigenberger, P. (2005). Impact of higher-order ionospheric terms on GPS estimates. *Geophysical Research Letters*, 32(23), L23311. <https://doi.org/10.1029/2005GL024342>
- Gelman, A., & Rubin, D. B. (1992). Inference from iterative simulation using multiple sequences. *Statistical Science*, 7(4), 457–472. <https://doi.org/10.1214/ss/1177011136>
- González Bonorino, G., Rinaldi, V., del Valle Abascal, L., Alvarado, P., Bujalesky, G. G., & Güell, A. (2011). Paleoseismicity and seismic hazard in southern Patagonia (Argentina-Chile; 50°–55°S) and the role of the Magallanes-Fagnano transform fault. *Natural Hazards*, 61(2), 337–349. <https://doi.org/10.1007/s11069-011-9917-2>



- Gourmelen, N., & Amelung, F. (2005). Postseismic Mantle Relaxation in the Central Nevada Seismic Belt. *Science*, 310(5753), 1473–1476. <https://doi.org/10.1126/science.1119798>
- Grant, L. B., & Sieh, K. (1994). Paleoseismic evidence of clustered earthquakes on the San Andreas Fault in the Carrizo Plain, California. *Journal of Geophysical Research*, 99(B4), 6819. <https://doi.org/10.1029/94jb00125>
- Griffiths, J. (2018). Combined orbits and clocks from IGS second reprocessing. *Journal of Geodynamics*, 93(2), 177–195. <https://doi.org/10.1007/s00190-018-1149-8>
- Hammond, W. C., Blewitt, G., & Kreemer, C. (2011). Block modeling of crustal deformation of the northern Walker Lane and Basin and Range from GPS velocities. *Journal of Geophysical Research*, 116(B4), B04402. <https://doi.org/10.1029/2010jb007817>
- Hanks, T. C., & Kanamori, H. (1979). A moment magnitude scale. *Journal of Geophysical Research*, 84(B5), 2348. <https://doi.org/10.1029/jb084ib05p02348>
- Ivins, E. R., & James, T. S. (2004). Bedrock response to Llanquihue Holocene and present-day glaciation in southernmost South America. *Geophysical Research Letters*, 31, L24613. <https://doi.org/10.1029/2004GL0215>
- Jacoby, G. C., Sheppard, P. R., & Sieh, K. E. (1988). Irregular recurrence of large earthquakes along the San Andreas Fault: Evidence from trees. *Science*, 241(4862), 196–199. <https://doi.org/10.1126/science.241.4862.196>
- Jaschek, E. U., Sabbione, N. C., & Sierra, P. J. (1982). Reubicación de sismos localizados en territorio argentino (1920–1963). *Serie de Geofísica*, XI(1). Retrieved from <http://sedici.unlp.edu.ar/handle/10915/85016>
- Johnston, G., Riddell, A., & Hausler, G. (2017). The International GNSS Service. In P. J. G. Teunissen, & O. Montenbruck (Eds.), *Springer handbook of global navigation satellite systems* (pp. 967–982). Springer International Publishing. [https://doi.org/10.1007/978-3-319-42928-1\\_33](https://doi.org/10.1007/978-3-319-42928-1_33)
- Kanamori, H. (1983). Magnitude scale and quantification of earthquakes. *Tectonophysics*, 93(3–4), 185–199. [https://doi.org/10.1016/0040-1951\(83\)90273-1](https://doi.org/10.1016/0040-1951(83)90273-1)
- Klepeis, K. A. (1994). The Magallanes and Deseado fault zones: Mayor segment of the South American-Scotia transform plate boundary in southernmost South America, Tierra del Fuego. *Journal of Geophysical Research*, 99(B11), 22001–22014. <https://doi.org/10.1029/94JB01749>
- Langbein, J. (2004). Noise in two-color electronic distance meter measurements revisited. *Journal of Geophysical Research: Solid Earth*, 109(B4), B04406. <https://doi.org/10.1029/2003jb002819>
- Lange, H., Casassa, G., Ivins, E. R., Schröder, L., Fritsche, M., Richter, A., & Dietrich, R. (2014). Observed crustal uplift near the Southern Patagonian Icefield constrains improved viscoelastic Earth models. *Geophysical Research Letters*, 41(3), 805–812. <https://doi.org/10.1002/2013gl058419>
- Lin, A., Kikuchi, M., & Fu, B. (2003). Rupture Segmentation and Process of the 2001 Mw 7.8 Central Kunlun, China, Earthquake. *Bulletin of the Seismological Society of America*, 93(6), 2477–2492. <https://doi.org/10.1785/0120020179>
- Liu-Zeng, J., Heaton, T., & DiCaprio, C. (2005). The effect of slip variability on earthquake slip-length scaling. *Geophysical Journal International*, 162(3), 841–849. <https://doi.org/10.1111/j.1365-246x.2005.02679.x>
- Lodolo, E., Menichetti, M., Bartole, R., Ben-Avraham, Z., Tassone, A., & Lippai, H. (2003). Magallanes-Fagnano continental transform fault (Tierra del Fuego, southernmost South America). *Tectonics*, 22(6), 1076. <https://doi.org/10.1029/2003TC001500>
- Lomnitz, C. (1970). Major earthquakes and tsunamis in Chile. *Geologische Rundschau*, 59(951). <https://doi.org/10.1007/BF02042278>
- Lozano, J. G., Bran, D. M., Donda, F., Lodolo, E., Esteban, F. D., & Tassone, A. (2021). “Palaeolago Fueguino”, a Late Pleistocene lacustrine basin located in the central sector of Tierra del Fuego: A seismostratigraphic study. *Journal of Quaternary Science*, 36(2), 273–287. <https://doi.org/10.1002/jqs.3276>
- Mann, P. (2007). Global catalogue, classification and tectonic origins of restraining- and releasing bends on active and ancient strike-slip fault systems. *Geological Society, London, Special Publications*, 290(1), 13–142. <https://doi.org/10.1144/sp290.2>
- Martinić Beroš, M. (2008). Registro Histórico de Antecedentes Volcánicos y Sísmicos en la Patagonia Austral y la Tierra del Fuego. *Magallania (Punta Arenas)*, 36(2). <https://doi.org/10.4067/s0718-22442008000200001>
- McCulloch, R., Fogwill, C., Sugden, D., Bentley, M., & Kubik, P. (2005). Chronology of the last glaciation in central Strait of Magellan and Bahía Inútil, southernmost South America. *Geografiska Annaler-Series A: Physical Geography*, 87(2), 289–312. <https://doi.org/10.1111/j.0435-3676.2005.00260.x>
- Meade, B. J., & Hager, B. H. (2005). Block models of crustal motion in southern California constrained by GPS measurements. *Journal of Geophysical Research: Solid Earth*, 110(B3), B03403. <https://doi.org/10.1029/2004JB003209>
- Meade, B. J., Klinger, Y., & Hetland, E. A. (2013). Inference of multiple earthquake-cycle relaxation timescales from irregular geodetic sampling of interseismic deformation. *Bulletin of the Seismological Society of America*, 103(5), 2824–2835. <https://doi.org/10.1785/0120130006>
- Mendoza, L., Perdomo, R., Hormaechea, J. L., Del Cogliano, D., Fritsche, M., Richter, A., & Dietrich, R. (2011). Present-day crustal deformation along the Magallanes-Fagnano Fault System in Tierra del Fuego from repeated GPS observations. *Geophysical Journal International*, 184(3), 1009–1022. <https://doi.org/10.1111/j.1365-246X.2010.04912.x>
- Mendoza, L., Richter, A., Fritsche, M., Hormaechea, J. L., Perdomo, R., & Dietrich, R. (2015). Block modeling of crustal deformation in Tierra del Fuego from GNSS velocities. *Tectonophysics*, 651–652, 58–65. <https://doi.org/10.1016/j.tecto.2015.03.013>
- Mendoza, L. P. O., Richer, A., Marderwald, E. R., Hormaechea, J. L., Connon, G., Scheinert, M., & Perdomo, R. A. (2021). *Time series of geocentric coordinates at geodetic sites for geodynamic studies related to the Magallanes-Fagnano Fault System in Tierra del Fuego*. PANGAEA. <https://doi.org/10.1594/PANGAEA.934034>
- Menichetti, M., Lodolo, E., & Tassone, A. (2008). Structural geology of the Fuegian Andes and Magallanes fold-and-thrust belt—Tierra del Fuego Island. *Geológica Acta*, 6(1), 19–42. Retrieved from <https://revistes.ub.edu/index.php/GEOACTA/article/view/104.000000239>
- Miles, P. (2019). pymcstat: A Python package for Bayesian inference using delayed rejection adaptive metropolis. *Journal of Open Source Software*, 4(38), 1417. <https://doi.org/10.21105/joss.01417>
- Miles, P. (2020). *prmls/pymcstat v1.9.1 [software]*. Retrieved from <https://zenodo.org/badge/latestdoi/107596954>
- Montillet, J.-P., & Bos, M. S. (Eds.). (2020). *Geodetic time series analysis in earth sciences*. Springer International Publishing. <https://doi.org/10.1007/978-3-030-21718-1>
- Okada, Y. (1992). Internal deformation due to shear and tensile faults in a half-space. *Bulletin of the Seismological Society of America*, 82(2), 1018–1040. <https://doi.org/10.1785/bssa0820021018>
- Pedraza, A., Galindo-Zaldívar, J., Ruiz-Constán, A., Bohoyo, F., Torres-Carbonell, P., Ruano, P., & González-Castillo, L. (2014). The last major earthquakes along the Magallanes-Fagnano fault system recorded by disturbed trees (Tierra del Fuego, South America). *Terra Nova*, 26(6), 448–453. <https://doi.org/10.1111/ter.12119>
- Pelayo, A. M., & Wiens, D. A. (1989). Seismotectonics and relative plate motions in the Scotia Sea region. *Journal of Geophysical Research: Solid Earth*, 94(B6), 7293–7320. <https://doi.org/10.1029/JB094iB06p07293>
- Perucca, L., Alvarado, P., & Saez, M. (2015). Neotectonics and seismicity in southern Patagonia. *Geological Journal*, 51(4), 545–559. <https://doi.org/10.1002/gj.2649>



- Piñón, D. A., Gómez, D. D., Smalley, R., Cimbaro, S. R., Lauría, E. A., & Bevis, M. G. (2018). The history, state, and future of the Argentine continuous satellite monitoring network and its contributions to geodesy in Latin America. *Seismological Research Letters*, 89(2A), 475–482. <https://doi.org/10.1785/0220170162>
- Rabassa, J., Coronato, A., & Martínez, O. (2011). Late Cenozoic glaciations in Patagonia and Tierra del Fuego: An updated review. *Biological Journal of the Linnean Society*, 103(2), 316–335. <https://doi.org/10.1111/j.1095-8312.2011.01681.x>
- Ray, R. D. (1999). *A Global Ocean Tide Model From TOPEX/POSEIDON Altimetry: GOT99.2*. (techreport No. 209478). NASA. Retrieved from <https://ntrs.nasa.gov/citations/19990089548>
- Rebeschung, P., & Schmid, R. (2016). IGS14/igs14.atx: A new framework for the IGS products. In *AGU fall meeting 2016*. Retrieved from <https://mediatum.ub.tum.de/1341338>
- Richter, A., Hormaechea, J. L., Dietrich, R., Perdomo, R. A., Fritsche, M., Del Coglioano, D., & Mendoza, L. P. O. (2010). Lake-level variations of lago fagnano, tierra del fuego: Observations, modelling and interpretation. *Journal of Limnology*, 69(1), 29. <https://doi.org/10.4081/jlimnol.2010.29>
- Roy, S., Vassallo, R., Martinod, J., Ghiglione, M. C., Sue, C., & Allemand, P. (2019). Co-seismic deformation and post-glacial slip rate along the Magallanes-Fagnano fault, Tierra Del Fuego, Argentina. *Terra Nova*, 32(1), 1–10. <https://doi.org/10.1111/ter.12430>
- Sabbione, N. C., Connon, G. C., Hormaechea, J. L., & Buffoni, C. (2007). *Tierra del Fuego Reference Standard Earthquake Catalogue (techreport) (FCAG, UNLP)*. Retrieved from <http://sedici.unlp.edu.ar/handle/10915/118869>
- Sabbione, N. C., Connon, G. C., Hormaechea, J. L., & Buffoni, C. (2017). *Complemento al Catálogo Sismológico de Referencia para Tierra del Fuego (techreport) (FCAG, UNLP)*. Retrieved from <http://sedici.unlp.edu.ar/handle/10915/119480>
- Sandoval, F. B., & De Pascale, G. P. (2020). Slip rates along the narrow Magallanes Fault System, Tierra Del Fuego Region. *Patagonia Scientific Report*, 10(1). <https://doi.org/10.1038/s41598-020-64750-6>
- Santibáñez, I., Cembrano, J., García-Pérez, T., Costa, C., Yáñez, G., Marquardt, C., & González, G. (2018). Crustal faults in the Chilean Andes: Geological constraints and seismic potential. *Andean Geology*, 46(1), 32. <https://doi.org/10.5027/andgeov46n1-3067>
- Sibson, R. H. (1989). Earthquake faulting as a structural process. *Journal of Structural Geology*, 11(1–2), 1–14. [https://doi.org/10.1016/0191-8141\(89\)90032-1](https://doi.org/10.1016/0191-8141(89)90032-1)
- Smalley, R., Kendrick, E., Bevis, M. G., Dalziel, I. W. D., Taylor, F., Lauría, E., & Piana, E. (2003). Geodetic determination of relative plate motion and crustal deformation across the Scotia-South America plate boundary in eastern Tierra del Fuego. *Geochemistry, Geophysics, Geosystems*, 4(9), 1070. <https://doi.org/10.1029/2002GC000446>
- Spade, D. A. (2020). Markov chain Monte Carlo methods: Theory and practice. In S. R. Arni, & C. R. Rao (Eds.), *Principles and methods for data science* (Vol. 43, pp. 1–66). Elsevier. <https://doi.org/10.1016/bs.host.2019.06.001>
- Stirling, M., Goded, T., Berryman, K., & Litchfield, N. (2013). Selection of earthquake scaling relationships for seismic-hazard analysis. *Bulletin of the Seismological Society of America*, 103(6), 2993–3011. <https://doi.org/10.1785/0120130052>
- Storchak, D. A., Harris, J., Brown, L., Lieser, K., Shumba, B., & Giacomo, D. D. (2020). Rebuild of the bulletin of the International Seismological Centre (ISC)—Part 2: 1980–2010. *Geoscience Letters*, 7(1). <https://doi.org/10.1186/s40562-020-00164-6>
- Tassone, A., Lippai, H., Lodolo, E., Menichetti, M., Comba, A., Hormaechea, J. L., & Vilas, J. F. (2005). A geological and geophysical crustal section across the Magallanes–Fagnano fault in Tierra del Fuego. *Journal of South American Earth Sciences*, 19, 99–109. <https://doi.org/10.1016/j.jsames.2004.12.003>
- Thomas, C., Livermore, R., & Pollitz, F. (2003). Motion of the Scotia Sea Plate. *Geophysical Journal International*, 115, 789–804. <https://doi.org/10.1111/j.1365-246X.2003.02069.x>
- Thomson, B. (2020). *Okada-wrapper v18.12.07.3 (software)*. Retrieved from <https://pypi.org/project/okada-wrapper/>
- Tong, X., Smith-Konter, B., & Sandwell, D. T. (2014). Is there a discrepancy between geological and geodetic slip rates along the San Andreas fault system? *Journal of Geophysical Research: Solid Earth*, 119(3), 2518–2538. <https://doi.org/10.1002/2013jb010765>
- van Dam, T. M., & Ray, R. (2010). *S1 and S2 atmospheric tide loading effects for geodetic applications*. Retrieved from <http://geophy.uni.lu/ggfc-atmosphere/tide-loading-calculator.html>
- Waldmann, N., Anselmetti, F. S., Ariztegui, D., Austin, J. A., Pirouz, M., Moy, C., et al. (2010). Holocene mass-wasting events in Lago Fagnano, Tierra del Fuego (54°S): Implications for paleoseismicity of the Magallanes-Fagnano transform fault. *Basin Research*, 23(2), 171–190. <https://doi.org/10.1111/j.1365-2117.2010.00489.x>
- Waldmann, N., Ariztegui, D., Anselmetti, F. S., Coronato, A., Austin, J. A. (2010). Geophysical evidence of multiple glacier advances in Lago Fagnano (54°S), southernmost Patagonia. *Quaternary Science Reviews*, 29(9–10), 1188–1200. <https://doi.org/10.1016/j.quascirev.2010.01.016>
- Wesnousky, S. G. (2008). Displacement and geometrical characteristics of earthquake surface ruptures: Issues and implications for seismic-hazard analysis and the process of earthquake rupture. *Bulletin of the Seismological Society of America*, 98(4), 1609–1632. <https://doi.org/10.1785/0120070111>
- Wessel, P., Luis, J. F., Uieda, L., Scharroo, R., Wobbe, F., Smith, W. H. F., & Tian, D. (2019). The generic mapping tools version 6. *Geochemistry, Geophysics, Geosystems*, 20(11), 5556–5564. <https://doi.org/10.1029/2019gc008515>
- Wright, T. J. (2016). The earthquake deformation cycle. *Astronomy and Geophysics*, 57(4), 420–426. <https://doi.org/10.1093/astrogeo/atw148>
- Wright, T. J., Elliott, J. R., Wang, H., & Ryder, I. (2013). Earthquake cycle deformation and the Moho: Implications for the rheology of continental lithosphere. *Tectonophysics*, 609, 504–523. <https://doi.org/10.1016/j.tecto.2013.07.029>
- Yamin, M. G., & Anselmi, G. (2020). Geología de las placas Scotia y Sandwich. In *Geología* (Vol. 8, p. 29). Instituto de Geología y Recursos Minerales, Servicio Geológico Minero Argentino. Retrieved from <https://repositorio.segemar.gov.ar/handle/308849217/4058>
- Zamarbide, J. L., & Castano, J. C. (1978). *Determinación de los coeficientes sísmicos zonales para la República Argentina (Tech. Rep. No. 6)*. Instituto Nacional de Prevención Sísmica (INPRES). Retrieved from [http://contenidos.inpres.gov.ar/docs/Reglamentos/INPRES-Pub\\_Tec\\_06.pdf](http://contenidos.inpres.gov.ar/docs/Reglamentos/INPRES-Pub_Tec_06.pdf)
- Zeng, Y., & Shen, Z. S. (2014). Fault network modeling of crustal deformation in California constrained using GPS and geologic observations. *Tectonophysics*, 612–613, 1–17. <https://doi.org/10.1016/j.tecto.2013.11.030>
- Zumberge, J. F., Heflin, M. B., Jefferson, D. C., Watkins, M. M., & Webb, F. H. (1997). Precise point positioning for the efficient and robust analysis of GPS data from large networks. *Journal of Geophysical Research: Solid Earth*, 102(B3), 5005–5017. <https://doi.org/10.1029/96jb03860>